Structural and mechanistic basis of the EMC-dependent biogenesis of distinct transmembrane clients

Lakshmi E. Miller-Vedam* [1,4,5,7], Bastian Bräuning* [2], Katerina D. Popova* [3,5,7], Nicole T. Schirle Oakdale [4,7,8], Jessica L. Bonnar [5,7], Jesuraj Rajan Prabu [2], Elizabeth A. Boydston [7,12], Natalia Sevillano [11,9], Matthew J. Shurtleff [7,10], Charles S. Craik [11], Brenda A. Schulman[# 2], Adam Frost[# 4], Jonathan S. Weissman[# 5,6,7]

*Authors contributed equally
[#] Co-corresponding

1. Molecular, Cellular, and Computational Biophysics Graduate Program, University of California, San Francisco, California, USA
2. Department of Molecular Machines and Signaling, Max Planck Institute of Biochemistry, Martinsried, Germany
3. Biomedical Sciences Graduate Program, University of California, San Francisco, California, USA
4. Department of Biochemistry & Biophysics, University of California, San Francisco, California, USA
5. Department of Biology, Whitehead Institute, MIT, Cambridge, Massachusetts, USA
6. Howard Hughes Medical Institute, USA
7. Department of Cellular and Molecular Pharmacology, University of California, San Francisco, California, USA
8. Current Address – Gilead Sciences, Foster City, California, USA
9. Current Address – FairJourney Biologics, Porto, Portugal
10. Current Address – Department of Bioengineering, Stanford University, California, USA
11. Department of Pharmaceutical Chemistry, University of California, San Francisco, California, USA.
12. Current Address –Whitehead Institute, MIT, Cambridge, Massachusetts, USA

**** Correspondence: schulman@biochem.mpg.de (B.A.S), Adam.Frost@ucsf.edu (A.F.), and weissman@wi.mit.edu (J.S.W.)**

Abstract

Membrane protein biogenesis in the endoplasmic reticulum (ER) is complex and failure-prone. The ER membrane protein complex (EMC), comprising eight conserved subunits, has emerged as a central player in this process. Yet, we have limited understanding of how EMC enables insertion and integrity of diverse clients, from tail-anchored to polytopic transmembrane proteins. Here, yeast and human EMC cryo-EM structures reveal conserved intricate assemblies and human-specific features associated with pathologies. Structure-based functional studies revealed at least two separable EMC activities, as an insertase regulating tail-anchored protein levels and as a polytopic membrane protein holdase chaperone. These depend on mechanistically coupled yet spatially distinct regions including two lipid-accessible membrane cavities which confer client-specific regulation, and a novel, non-insertase EMC function mediated by the EMC lumenal domain. Our studies illuminate the structural and mechanistic basis of EMC's multifunctionality and point to its role in differentially regulating the biogenesis of distinct client protein classes.

Introduction

Integral membrane proteins serve diverse and critical cellular roles, including signal transduction, lipid biosynthesis, adhesion, and transport of molecules across the bilayer. In eukaryotic cells, the endoplasmic reticulum (ER) serves as the primary site of integral membrane protein synthesis, targeting (co- or post-translationally), insertion, folding and quality control (Ellgaard 2016; Costa, 2018). However, the features of membrane-spanning regions (e.g. low hydrophobicity, charged residues, non-optimal lengths, lipid- and ion-binding sites and hairpins or kinked transmembrane helices) that mediate important functions pose particular challenges for transmembrane protein biosynthesis and folding. Consequently, membrane protein biogenesis is prone to failure, and this can lead to cellular stress and disease (Marinko, 2019). Thus, it is important to understand the cellular factors that facilitate proper membrane protein biogenesis for such challenging clients.

The ER membrane protein complex (EMC) has emerged as a conserved player in the process of membrane protein biogenesis. It was first identified in *Saccharomyces cerevisiae,* as an abundant and stable multi-protein membrane complex whose disruption results in stress mirroring that caused by misfolded membrane proteins (Jonikas, 2009). Loss of the EMC in mammalian cells is associated with failed biogenesis and degradation of a subset of membrane proteins (Christianson, 2012). Accordingly, the EMC has been implicated in several mechanistically distinct steps of membrane protein biogenesis, stabilization, and quality control (Bircham, 2011; Richard, 2013; Satoh, 2015; Savidis, 2016; Shurtleff and Ithzak, 2018; Volkmar, 2018; Tian, 2019).

One well-established EMC function is as an insertase for terminal transmembrane helices. EMC's insertase function has been demonstrated for two classes of clients: low hydrophobicity tail-anchored proteins (i.e. those that contain C-terminal membrane anchors) and a subset of polytopic transmembrane proteins in which the first helix is inserted with the

N-terminus in the lumen (Guna, 2018; Chitwood, 2018). However, many studies indicate EMC functions beyond initial insertion of N- or C-terminal helices. The EMC has been implicated in the biogenesis and stability of many membrane protein classes that do not require a terminal transmembrane insertase (Bircham, 2011; Louie, 2012; Richard, 2013; Shurtleff and Ithzak, 2018; Coelho, 2019; Luo, 2002; Volkmar, 2018; Talbot, 2019; Petkovic, 2020). Recent studies have shown that the EMC is required for stability of internal transmembrane helices of human and viral multi-pass membrane proteins (Hiramatsu, 2019; Lin 2019; Ngo, 2019; Coelho, 2019; Xiong, 2020). Additionally, the human EMC (hEMC) physically interacts with the NS4A-B region of the Dengue Virus polyprotein following Sec61-dependent translocation and signal peptidase cleavage, suggesting roles in post-translational stabilization of polytopic membrane proteins (Ngo, 2019; Lin 2019). Similarly, the *S. cerevisiae* EMC (yEMC) co-immunoprecipitated with full-length polytopic transmembrane clients, including Pma1p (Luo, 2002), Mrh1p, and Fks1p (Shurtleff and Ithzak, 2018). In addition to varying types of transmembrane protein clients, the EMC also associates with a range of regulatory factors, including many general and substrate-specific chaperones in the cytoplasm and in the ER lumen (Bagchi, 2016; Coelho, 2019; Kudze, 2018; Richard, 2013; Shurtleff and Ithzak, 2018).

The complex architecture of the EMC provides additional support for multifunctionality in membrane protein biogenesis. The EMC is an eight (yeast) or nine (mammalian) component, 248-284 kDa complex with considerable mass in the ER lumen, membrane and cytosol. The cytoplasmic domain contains conserved tetratricopeptide repeats (TPR) repeats in EMC2, and the human complex accommodates an additional subunit, EMC8/9, whose function is not yet understood. The ER lumenal domain in yeast does not contain an N-terminal EMC1 expansion seen in hEMC. Notably, the ER lumenal domain has been linked to a number of disease-associated phenotypes (Junes-Gill, 2010; Probert, 2015; Harel, 2016; Abu-Safieh, 2012; Diamantopoulou, 2017; Marquez, 2020), and presents the possibility of additional functions for the human lumenal domain. One EMC subunit (EMC3) shares limited sequence homology with a family of insertases that are evolutionarily related to the bacterial insertase YidC (Samuelson, 2000; Kumazaki, 2014; Borowska, 2015; Anghel, 2017), perhaps explaining the insertase function of the complex. Nonetheless, the elaboration of the EMC compared to other known TMD insertases and a diverse client range suggest additional functionality that has so far eluded mechanistic explanation.

Here, we determined high-resolution cryoEM structures of yeast and human EMC and characterized the phenotypes of three distinct classes of EMC clients associated with a series of structure-based EMC mutants. Both yEMC and hEMC structures reveal a path for transmembrane helix insertion from the cytoplasm into the membrane via a conserved cavity. Our structures and mutants also revealed a second lipid-filled cavity with regions of importance for all three client types probed. Analysis of human disease mutations in EMC1 and our structure-informed mutations enabled us to decouple the EMC insertase function from non-insertase functions and reveal a potential role of the EMC in differentially controlling the biogenesis of distinct classes of client proteins. These structure-function studies collectively establish that the EMC adopts a modular architecture enabling its diverse functions in membrane protein biogenesis.

Results

Overview of strategy to comprehensively reveal EMC structure and function

To comprehensively dissect both conserved and species-specific functions of the EMC, we developed approaches to produce EMC for structure determination and broad mutational analysis (**Figure 1**). We developed systems to produce robust quantities of pure intact yEMC and hEMC to determine structures for the two organisms in which different facets of EMC function have been described in detail (Jonikas, 2009; Christianson, 2012; Guna, 2018; Shurtleff and Ithzak, 2018). Parallel efforts converged on an approach involving FLAG affinity-tagging of the EMC5 C-terminus, which was performed for endogenous yEMC and fully recombinant hEMC in human embryonic kidney (HEK) cells (**Figure 1 – figure supplement 1-2**).

In parallel, to enable testing of hypotheses based on structures, we created a suite of human (K562) knockout cell lines deleted for individual EMC subunits - EMC1 (lumen), EMC2 (cytoplasm), EMC3 and EMC5 (transmembrane) - and a series of reporters of EMC-dependent transmembrane protein biogenesis (**Figure 1 – figure supplement 3**). Reintroduction of the wildtype EMC subunits in the respective knockout cells fully rescued the knockout phenotype (**Figure 1 – figure supplement 4-5**). This allowed for introduction of structure-based mutations in EMC subunits into the respective knockout cells to determine features supporting biogenesis of fluorescently-tagged versions of three different types of EMC clients: a C-terminal tail-anchored transmembrane protein (squalene synthase, SQS) (Guna, 2018), a polytopic transmembrane protein that depends on the EMC N-terminal insertase activity (Beta 1 adrenergic receptor, B1AR) (Chitwood, 2018), and a polytopic transmembrane protein (Sigma intracellular receptor 2, TMEM97) whose biogenesis requires the Sec61 translocon but does require a terminal helix insertase (**Figure 1 – figure supplement 3-7**). Monitoring the effect of an EMC mutation on fluorescent reporter levels provided a quantitative measure of its impact on EMC-dependent biogenesis of each class of client protein. Western blots against the endogenous EMC subunits allowed us to control for mutational effects on the production and stability of the EMC complex itself (**Figure 1 – figure supplement 4-5**). This strategy thus distinguishes effects resulting from a global disruption of the EMC complex from those caused be specific disruption of one or more EMC functions.

FIGURE 1

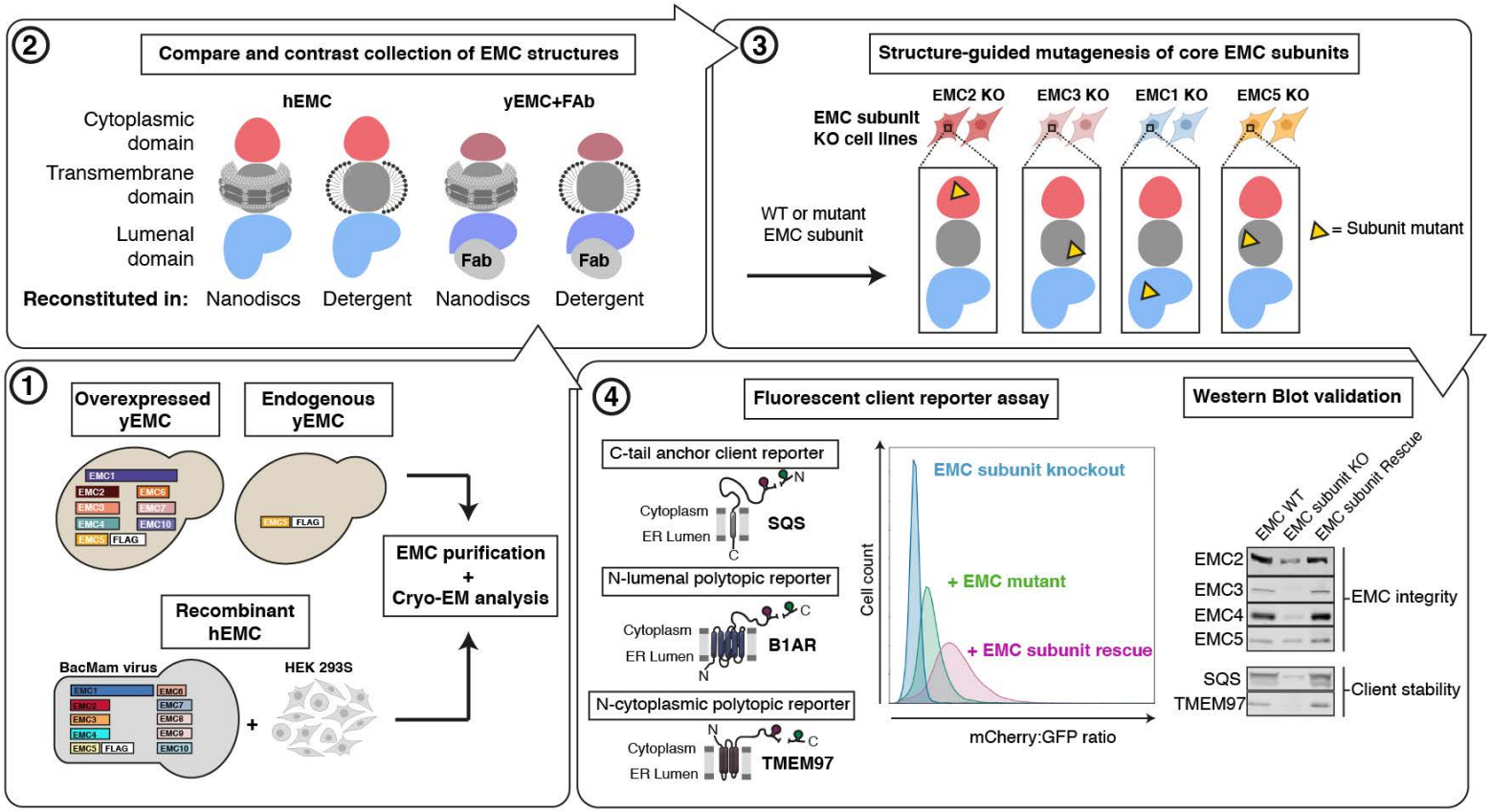

Figure 1: **Experimental strategy for the dissection of EMC function.**
Schematic representation of the combined structural and mutational approach to dissect EMC function.
(1) yEMC was expressed either by overexpression of all subunits together with Flag-tagged EMC5 or by endogenous expression from a genomic Flag-tagged EMC5 strain. For hEMC, all subunits were overexpressed together with Flag-tagged EMC5 via a single recombinant BacMam virus. EMC was purified by column chromatography and subjected to cryo-EM analysis.
(2) The obtained collection of cryo-EM structures of yEMC and hEMC in nanodiscs or detergent were compared to identify similarities and differences.
(3) Structure-guided mutagenesis was performed across four core EMC subunits: EMC1, EMC2, EMC3, and EMC5.
(4) Each EMC subunit knock-out (KO) cell line was individually transduced with three different fluorescent client reporters: C-terminus of SQS, full length B1AR, and full length TMEM97. Mutant EMC subunits were introduced into KO cell lines missing the corresponding EMC subunit in each of the three fluorescent EMC client reporter cell lines. EMC client stability in each mutant EMC subunit cell line was assessed by fluorescent cell sorting and quantifying the mCherry-to-GFP ratio. Western blotting was performed for each mutant-transduced cell line to assess EMC integrity (by immunoblotting for core EMC subunits) as well as client stability (by immunoblotting for EMC clients) and compared against both wild-type (WT) and KO cell lines.

176 **The EMC is an intricate molecular machine spanning the ER membrane and exhibits a**
177 **conserved core architecture**
178
179 We determined structures of yEMC and hEMC — all showing overall compositional
180 similarity, yet regional conformational differences between the yeast and human complexes
181 (**Figure 2**). We obtained reconstructions of yEMC bound to an antigen binding fragment
182 (Fab) and hEMC reconstituted both in detergent micelles and lipid nanodiscs, with the latter
183 strategy yielding the most isotropic and highest resolution data. For yEMC+FabDH4 and
184 hEMC, the global map resolutions reached 3.2 Å and 3.4 Å, respectively (**Figure 2 – figure**
185 **supplement 1 - 4**). The cryo-EM maps allowed for *de novo* model building of both human
186 and yeast complexes (**Figure 2 – figure supplement 5, 6**). We note that our maps and models
187 are consistent with recent cryo-EM data from yeast EMC (Bai, 2020), human EMC
188 (O'Donnell, Phillips, and Yagita, 2020; Pleiner, Tomaleri, and Januszyk, 2020), and a crystal
189 structure of human EMC2-EMC9 (O'Donnell, Phillips, and Yagita, 2020) published while we
190 were in the final stages of manuscript preparation. As described in the following sections, our
191 multiple EMC structures enable a broad survey of its conserved architecture, with variations
192 between the structures pointing to conformational and compositional differences (**Figure 2 –**
193 **figure supplement 7**).
194
195 The EMC comprises cytoplasmic, transmembrane and lumenal domains arranged similarly
196 for yeast and human, despite significant evolutionary separation (**Figure 2A-B**). For both
197 species, subunits encompassing EMC2 to EMC7 form an interconnected core complex, while
198 there is additional density capping both the cytoplasmic and lumenal domains of hEMC,
199 occupied by an EMC8/9 and an EMC1 N-terminal expansion, respectively (**Figure 2C-D**).
200 EMC8 and EMC9 are paralogs of each other, which have not been identified in yeast
201 (Wideman, 2015). We modeled and depict only EMC8 for clarity, but due to the 44%
202 sequence identity with EMC9 and both being present in the recombinant system we refer to
203 this as EMC8/9. The large EMC1 insertion in hEMC constitutes the majority of a membrane
204 distal beta-propeller domain protruding into the lumen, a feature missing from *S. cerevisiae*.
205 Compared to other ER-resident proteins (Suloway, 2009; Pfeffer, 2017; Ramírez, 2019), the
206 arrangement of domains of the EMC is unusual with the transmembrane domain connecting
207 prominent cytoplasmic and lumenal domains (**Figure 2E)**. On a global level, the structure
208 suggests complexities beyond those of some other ER machineries fulfilling select functions
209 in transmembrane protein biogenesis.
210

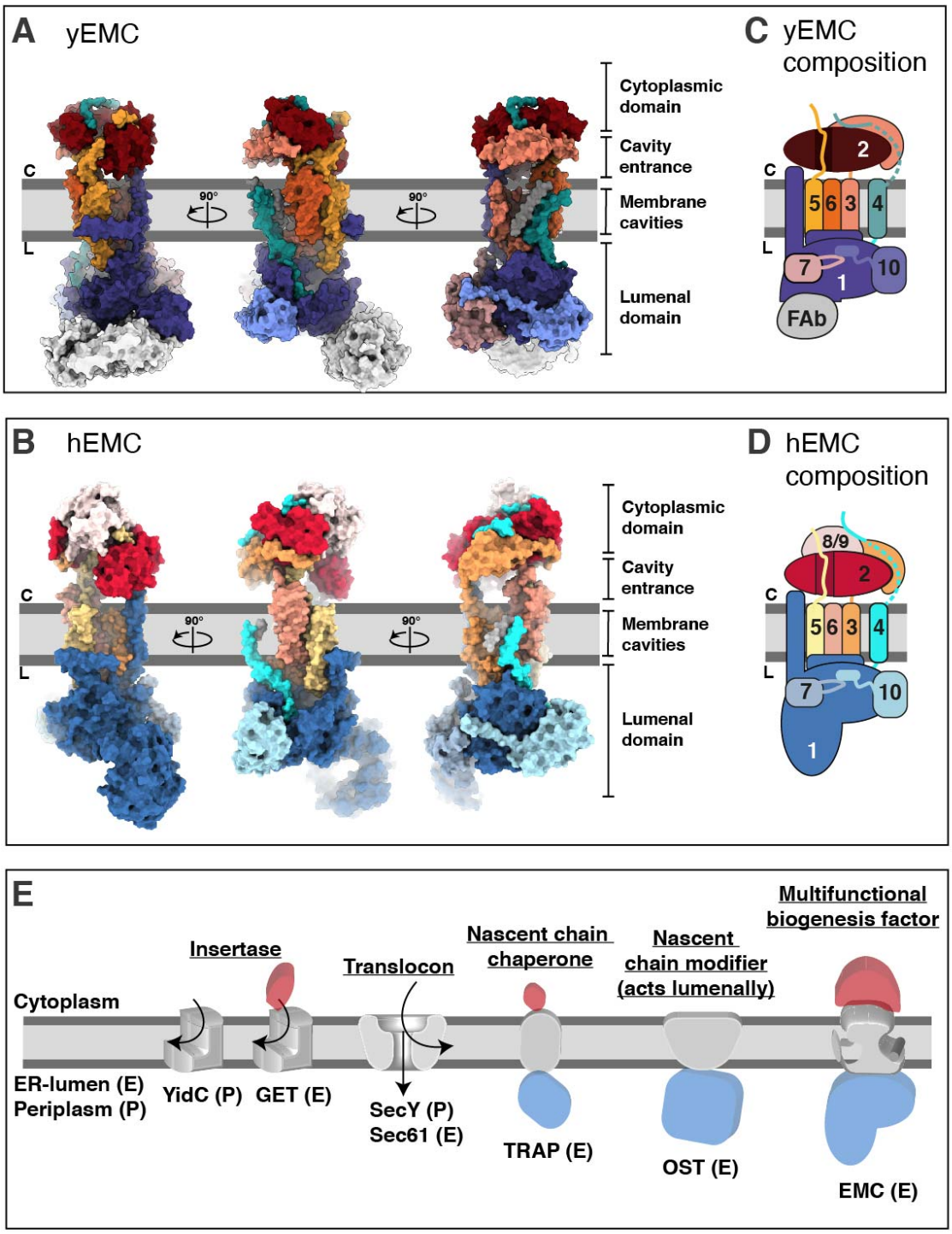

Figure 2: **Overall structures of yeast and human EMC.**

A) Cryo-EM structure of yEMC in nanodiscs. Three orthogonal views of the yEMC cryo-EM structure shown as surface rendering. Grey bars delineate the approximate ER membrane boundaries with the cytoplasmic (C) and lumenal (L) sides indicated. The FAb molecule bound to the yEMC1 lumenal domain is colored in grey.

B) Cryo-EM structure of hEMC in nanodiscs. Labeling as in A).

C) Subunit composition and color scheme of yEMC used throughout the manuscript. Dotted line indicates a portion of EMC4 unresolved in the cryo-EM map and left unmodeled.

D) Subunit composition and color scheme of hEMC used throughout the manuscript.

E) Schematic depiction and comparison of the EMC architecture to known transmembrane protein biogenesis factors in the ER and the bacterial plasma membrane. Cytoplasmic, transmembrane and lumenal domains are depicted as cartoons colored red, grey and blue, respectively. E, eukaryotic; P, prokaryotic.

211
212

The cytoplasmic domain provides a platform for protein-protein interactions

The exterior interface of the cytoplasmic domain is formed by EMC2, EMC3, EMC4, and parts of EMC8/9 (in human), while parts of EMC5, EMC2, and EMC8/9 are shielded from the cytoplasm (**Figure 3A-B; Figure 2 – figure supplement 7**). The helical fold of EMC2 constitutes the central organizer of this platform, established by five or six TPR motifs in human versus yeast, respectively (**Figure 3C**). TPR domains are commonly found mediating protein-protein interactions, and are present in numerous well-characterized chaperone-protein and other interaction networks (Blatch, 1999; Scheufler, 2000; Schlegel, 2007; Assimon, 2015; Krysztofinska, 2017; Graham, 2019). Yeast EMC2 features a more curved helical arrangement with N- and C-terminal domains in closer proximity to each other than seen in human EMC2. Notably, the canonical peptide-binding TPR groove is occupied by the partially helical C-terminus of EMC5, which forms a large interaction surface with EMC2. To test the functional roles of this interaction, we mutated three residues within the EMC2 TPR motif (hEMC2$^{K125E + R126D + K127E}$) or a single EMC5 residue buried in the TPR binding groove (hEMC5^{F90A}). The mutations on both sides of the interface decreased EMC integrity, with a modest (for the single point mutation) and significant (for the multi-residue mutation) reduction in the levels of several EMC subunits (**Figure 3C, Figure 3 – figure supplement 1-2, Figure 1 – figure supplement 4-5**). This suggests that this interface might be critical for EMC complex assembly rather than activity (e.g. client binding).

The multi-protein cytoplasmic cap has distinct elements between hEMC and yEMC. Capping the cytoplasmic domain in hEMC is EMC8/9 (**Figure 3 – figure supplement 3**), the functional roles of this cap-like structure are not yet clear. A groove on EMC8/9 cradles an N-terminal peptide of EMC4, which proceeds into the EMC4 segment that traverses over EMC2 and the three-helix bundle of EMC3 (**Figure 3D**). Though yEMC lacks EMC8/9, yeast EMC4 follows a similar binding trajectory along cytoplasmic EMC2 and EMC3 surfaces. We mutated two patches of EMC2 residues in proximity to the EMC4 cytoplasmic region (hEMC2$^{E146A+E149A+Q150A}$, hEMC2$^{E168A+D170A+K173A}$), which led to a modest accumulation of the tail-anchored client (SQS) but did not affect polytopic client abundance or decrease abundance of EMC subunits (**Figure 3E-G, Figure 1 – figure supplement 4-5**). Several mutants across the cytoplasmic domain showed similar phenotypes, supporting a key role in tail anchor protein biogenesis (**Figure 3 – figure supplement 1-2**).

FIGURE 3

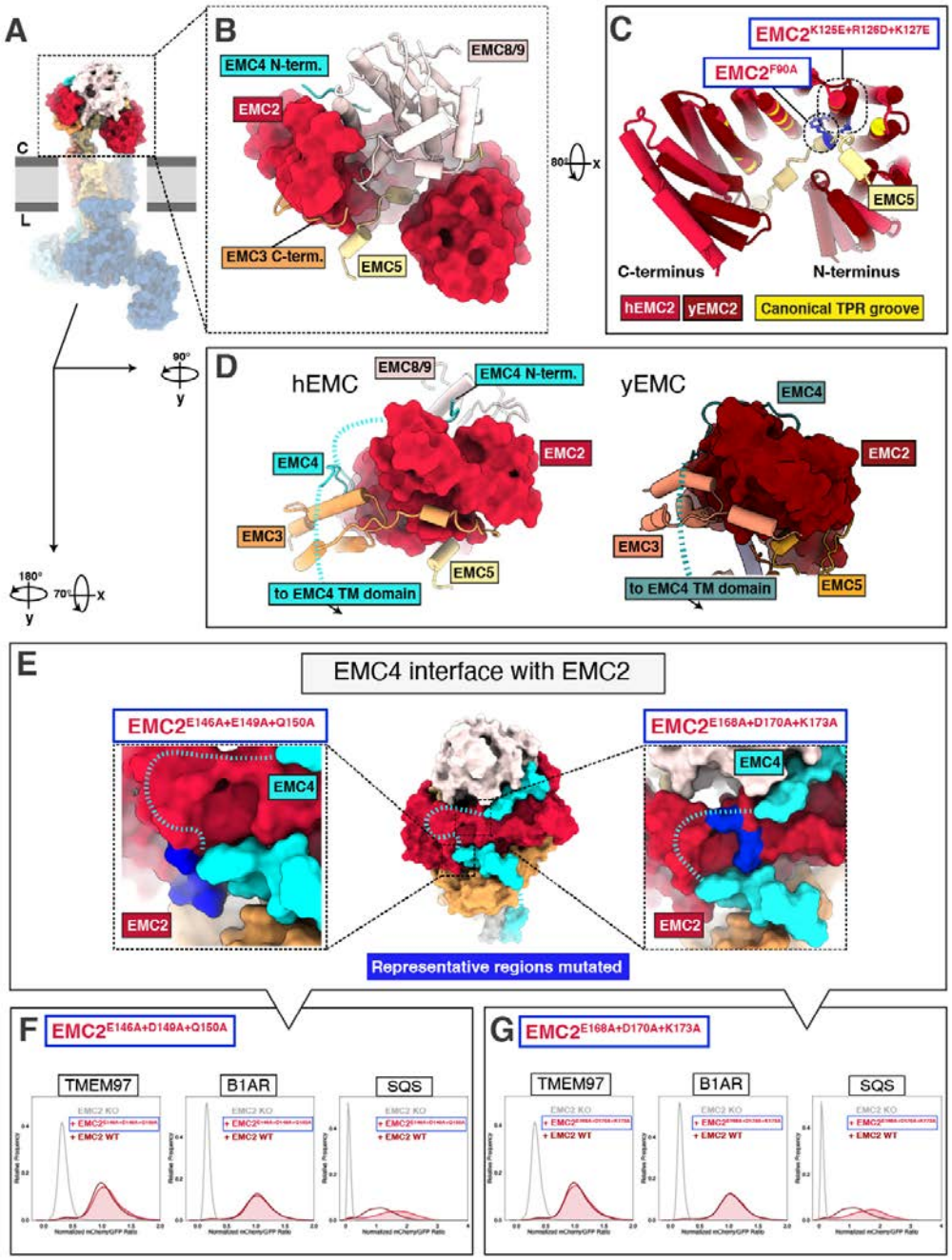

Figure 3: **The EMC cytoplasmic domain contains conserved functional interfaces and may engage C-tail anchored clients directly.**

A) Position of the hEMC cytoplasmic domain relative to the membrane and the rest of the complex. Shown is the surface rendered hEMC structure reconstituted in nanodiscs.

B) EMC2 nucleates a protein-protein interaction hub in the cytoplasm. Zoomed-in view of the cytoplasmic domain from A). EMC2 is shown as surface rendering while interacting EMC subunits are shown as cartoon cylinders.

C) EMC2 forms a TPR domain which binds EMC5. Overlaid are hEMC2 (red) and yEMC2 (dark red), illustrating the more tightly wound yEMC2 TPR solenoid. Canonical residues lining the concave TPR interior are colored in yellow stripes on the dark red for hEMC2. Two mutants, one in EMC5 and three in EMC2, are colored in blue, and show destabilizing phenotypes for EMC integrity.

D) A cytoplasmic cap structure involving EMC4 is conserved in yEMC and hEMC. Shown is a side-by-side comparison between the cytoplasmic domains of hEMC (left) and yEMC (right), highlighting the similar path EMC4 takes from the cytoplasmic domain towards the transmembrane domain. While an interaction surface between EMC8/9 and the EMC4 N-terminus is absent in yeast, yEMC4 binds at the top of the EMC2 TPR domain and assumes as similar position across the EMC3 cytoplasmic domain at the cytoplasm-membrane interface.

E) Location of two EMC2-EMC4 interfaces targeted for mutagenesis. hEMC is shown as surface rendering with the mutated EMC2 regions highlighted in blue.

F) Fluorescent client reporter stability assay for TMEM97 (N-cytoplasmic polytopic client), B1AR (N-lumenal polytopic client) and SQS (C-lumenal tail-anchored client) in EMC2 KO cells expressing mutant hEMC2$^{E146A+D149A+Q150A}$ (shaded) or WT hEMC2 rescue (unshaded).

G) Fluorescent client reporter stability assay, as in F, for the hEMC2$^{E168A+D170A+K173A}$ mutant.

246 **Two distinct cavities are present in the transmembrane domain**
247
248 The transmembrane core of EMC is predicted to include contributions from each subunit
249 except for EMC2 and, in humans, EMC8/9 (**Figure 2C-D**). The EMC presents two distinct
250 and structurally conserved cavities on opposite sides of the transmembrane core that differ in
251 size, shape, subunit compositions and apparent function (**Figure 4A-B**). One cavity, which we
252 refer to as the lipid-filled cavity, appears contiguous with the ER lipid environment (**Figure**
253 **4A**). The second cavity, which we refer to as the gated cavity, appears to open towards the
254 cytoplasm in our structures and is more occluded by a transmembrane helix gate from the
255 lipid environment (**Figure 4B**). Notable structural hallmarks present in both species include a
256 superimposable core of nine transmembrane helices, a set of flexible gate helices, and an
257 amphipathic EMC1 brace helix (**Figure 4C**).
258

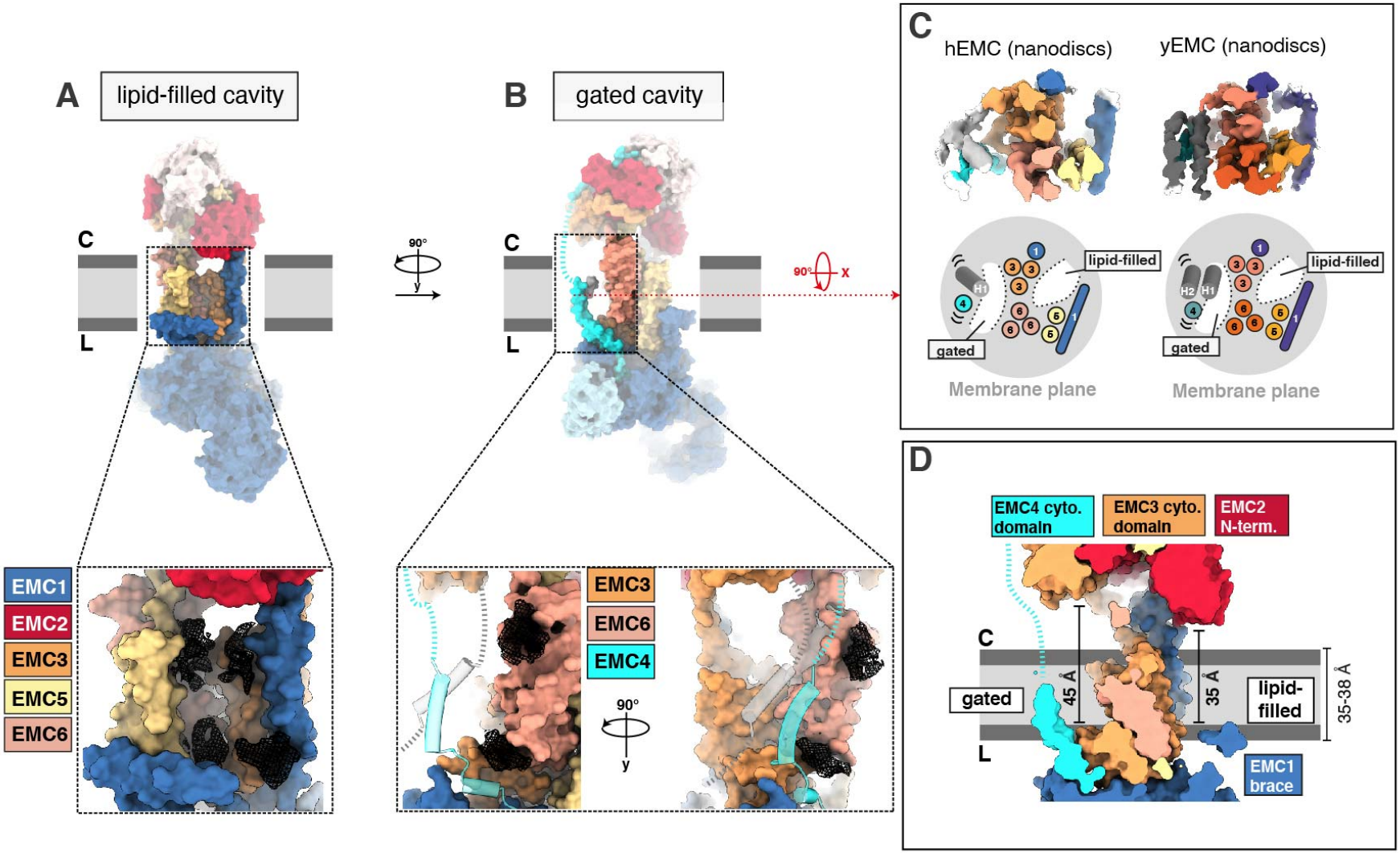

Figure 4: **The EMC houses two transmembrane cavities with conserved core structures and distinct accessibilities.**

A) Location and composition of the lipid-filled cavity. A zoom-in view on the cavity is shown below, which is composed of EMC1, EMC3, EMC5 and EMC6. Resolved lipid densities from the cryo-EM map of hEMC in POPC nanodiscs are shown as black mesh zoned within 3 Å of modeled POPC molecules.

B) Location and composition of the gated cavity. Two orthogonal zoom-in views of the cavity are shown below, which is composed of EMC3 and EMC6. A transmembrane gate opposite the cavity wall is depicted as transparent cartoon cylinders and has contributions from the C-terminal EMC4 transmembrane helix along with up to two additional, unassigned helices. Resolved lipid densities are shown as in A).

C) The dual-cavity architecture of the EMC transmembrane domain is conserved between yEMC and hEMC. Unsharpened cryo-EM maps of hEMC and yEMC in nanodiscs (top) are shown along with corresponding schematic representations of the spatial organization of all transmembrane helices (bottom). The gate helices of the gated cavity represent the region of highest conformational heterogeneity across our collection of EMC structures.

D) The two EMC transmembrane cavities feature distinct accessibilities. Shown is a central slice through the surface rendered hEMC nanodisc structure with the two membrane cavities on opposite sides. Measuring from the lumenal to the cytoplasmic side, gated and lipid-filled cavities measure 45 Å and 35 Å across, respectively. This suggests that the gated cavity has accessibility from the cytoplasm while the lipid-filled cavity does not.

259 **The gated cavity serves as a conduit for terminal helix insertion**
260
261 Evaluating potential client paths from the cytoplasm into the transmembrane domain revealed
262 a cavernous opening at the membrane-cytoplasmic interface of the gated cavity, wide enough
263 to allow passage of a client helix, and tapering towards the lumen (**Figure 4D)**. Consistent
264 with its potential role as a cytoplasmic conduit into the EMC, the EMC3 portion of the
265 cytoplasmic domain, which delineates this opening, sits approximately 45 Å from the lumenal
266 side of the gated cavity. This dimension exceeds the thickness of the ER membrane (Mitra,
267 2004; Heberle, 2020; Cornell, 2020) (**Figure 4D**). This cavity is lined primarily by EMC3,
268 EMC4 and EMC6 (**Figure 5A**). Simulating the dimension of the first transmembrane helix of
269 a known terminal insertase-client (B1AR, Chitwood, 2018) suggests that there is sufficient
270 space for a client helix even in the client-free state of the EMC (**Figure 5B**). The gated cavity
271 is hydrophilic on the cytoplasmic side and becomes increasingly hydrophobic towards the
272 lumenal side (**Figure 5C**).
273
274 The entrance into the gated cavity interior (**Figure 5A**) is formed primarily by the EMC3
275 cytoplasmic domain. To test its function, charge swap mutations were introduced along the
276 rim of this opening (hEMC3$^{E63K + D213K + E223K}$, hEMC3$^{R59E + R62E + K216E}$) (**Figure 5D, Figure 5**
277 **– figure supplement 2**). These mutants resulted in loss of the tail-anchored client (SQS) and
278 partial loss of the N-terminal insertase dependent polytopic client (B1AR), reflecting a failure
279 to support insertase activity. These mutants had no appreciable effect on the abundance of the
280 polytopic transmembrane client (TMEM97) reporter (**Figure 5E, Figure 5 – figure**
281 **supplement 1-2**). A similar phenotype was observed with alanine substitutions for a pair of
282 lysines at the periphery of this cytoplasmic rim (hEMC3$^{K42A + K43A}$) (**Figure 5 – figure**
283 **supplement 2**).
284
285 Having identified a functionally important entry route for terminal helix insertase clients, we
286 next considered potential surfaces inside the cavity that might accommodate a client helix. A
287 polar patch close to the membrane interior of this cavity was conspicuous, even though the
288 specific amino acid residues are not strictly conserved (**Figure 5 - figure supplement 2,**
289 **Figure 1 – figure supplement 7**). Mutating a pair of adjacent asparagine residues to
290 equivalently sized but negatively charged aspartates (hEMC3$^{N114D+N117D}$) resulted in a
291 dramatic decrease in SQS and a mild decrease in the polytopic terminal insertase client
292 (B1AR) (**Figure 5F**). Meanwhile, mutating a neighboring positively charged residue to an
293 alanine (hEMC3^{R180A}), a residue that is conserved in some of the YidC-superfamily insertase
294 proteins (**Figure 5 – figure supplement 4**) (Anghel, 2017), resulted in partial loss of only the
295 tail-anchored insertase client (SQS) (**Figure 5 - figure supplement 1**).
296

297 Lastly, we surveyed residues closer to the hydrophobic lumenal side of the gated cavity. Lipid
298 density was resolved at positions along the cavity in hEMC and yEMC cryo-EM maps
299 (**Figure 4B**) and the properties of this hydrophobic seal to the lumen are conserved (**Figure 5**
300 **- figure supplement 2**). The importance of this hydrophobic seal is suggested by the strong
301 effect of a structurally-mild mutation of a conserved methionine to a leucine (hEMC3^{M151L}),
302 which caused significant decrease in both SQS and B1AR abundance (**Figure 5G**). Mutation
303 of a neighboring aromatic residue (hEMC3^{F148L}), contacting both a lipid and the EMC4 C-
304 terminal transmembrane helix, caused a marked decrease in all three client types without
305 altering the levels of EMC subunits (**Figure 5 – figure supplement 1-2, Figure 1 – figure**
306 **supplement 7**). Together these results indicate that proper EMC insertase function depends
307 on the exact composition of the cavity and not simply on its hydrophobic nature.
308

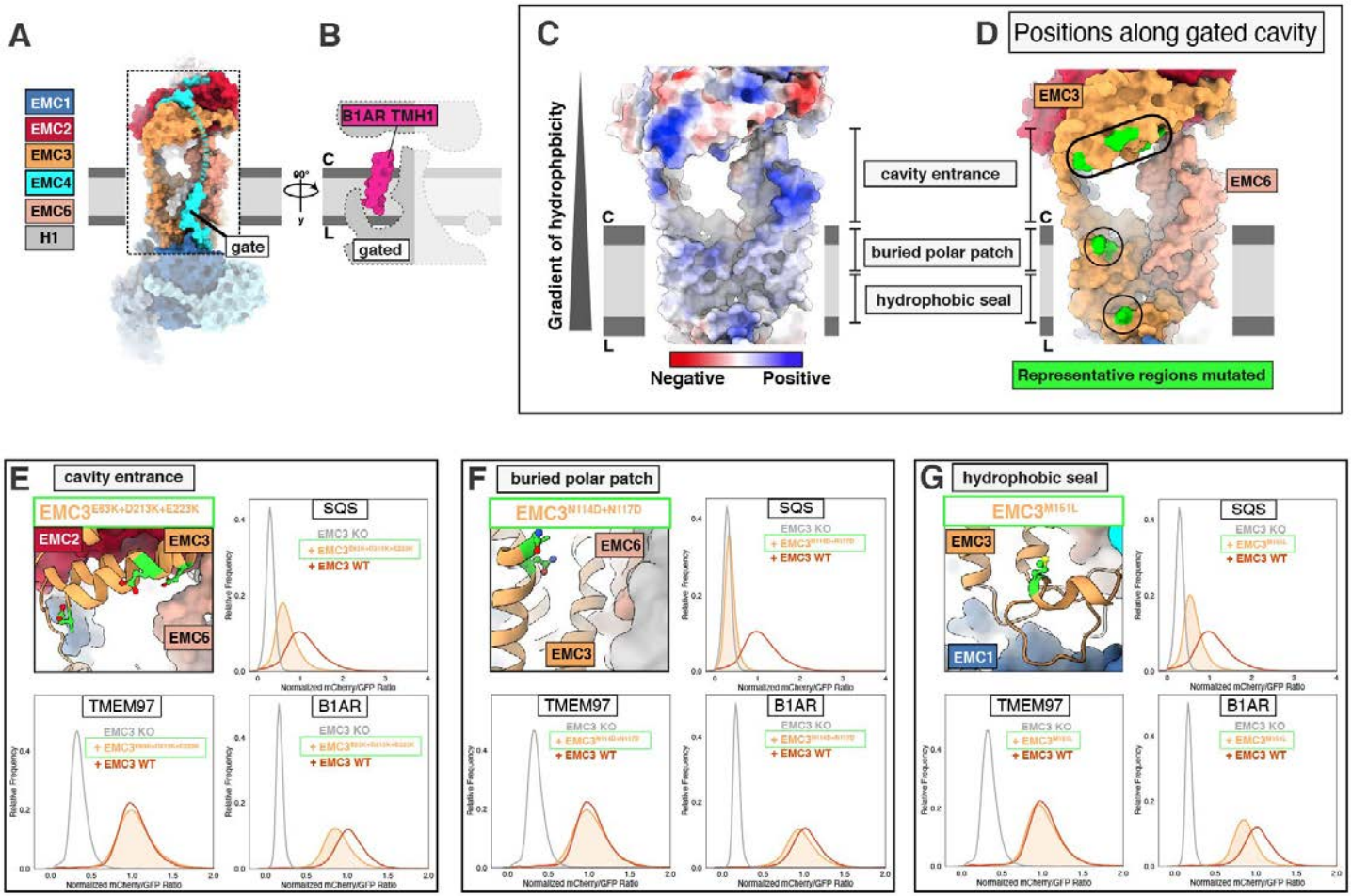

Figure 5: **EMC houses an insertase module centered on EMC3 in the gated membrane cavity.**

A) A transmembrane gate anchored in the cytosol and the lumen is a structural hallmark of the EMC gated cavity. Shown is a surface rendering of the hEMC model in nanodiscs with an unresolved EMC4 connection between the cytoplasm and the membrane depicted as a dashed line. An unassigned helix of the gate is shown in gray (H1).

B) The gated cavity in the hEMC nanodisc structure has sufficient space to accommodate a client transmembrane helix. The space-filling model of the first transmembrane helix of B1AR (B1AR TMH1) is shown placed inside an outline of the gated EMC cavity.

C) A hydrophobic gradient characterizes the surface of the EMC gated cavity from the cytoplasmic to the lumenal side. Gate helices have been omitted for clarity. The surface of the hEMC nanodisc structure is colored by electrostatic surface potential ranging from -15 (red) to +15 (blue) kcal/(mol·*e*).

D) Distinct EMC3 regions along the gated cavity hydrophobic gradient targeted for mutagenesis. A selection of mutated residues are colored in lime.

E) Fluorescent client reporter stability assay for the EMC3 cavity entrance mutant, hEMC3$^{E63K+D213K+E223K}$. A zoom-in on the mutated residues (colored lime) is shown in the top-right panel.

F) As in E) for the EMC3 buried polar patch mutant, hEMC3$^{N114D+N117D}$.

G) As in E) for the EMC3 hydrophobic seal mutant, hEMC3^{M151L}.

309 **Structural heterogeneity suggests a role for the gate in regulating access to the insertase**
310 **transmembrane cavity**
311
312 While the core transmembrane helices of the gated cavity are superimposable in all four of
313 our EMC structures, the adjacent gate helices appear in different relative orientations. The
314 structural variability likely reflects dynamics of the gate (**Figure 4C**). Comparing detergent
315 and nanodisc maps for both species identified two major gate conformations [**Video 1].** One
316 of the conformations, referred to as the closed gate conformation, results in a more occluded
317 membrane cavity. The other conformation, referred to as the open gate conformation, would
318 provide space for client accommodation.
319
320 The C-terminal transmembrane helix of EMC4 and ensuing lumenal segment are well
321 resolved in all four structures; however, other regions of EMC4, including the segment
322 connecting the cytoplasmic domain to the transmembrane gate helices, were poorly resolved
323 perhaps owing to mobility. The yEMC detergent map, yEMC nanodisc map, and hEMC
324 detergent map all show the unassigned helices in the closed conformation, preventing client
325 residence in the gated cavity. By contrast, the hEMC nanodisc map reveals an open gate
326 conformation with the unassigned helices shifted away from the transmembrane core to
327 provide space for a client (**Figure 5B**). We note that the conformational heterogeneity and
328 concomitant lower resolution of the gate likely accounts for the challenges in making
329 unambiguous subunit assignments (**Figure 5 – figure supplement 3**), reflected by the three
330 different interpretations reported in recent structures (Pleiner, Tomaleri, and Januszyk, 2020;
331 O'Donnell, Phillips, and Yagita, 2020; Bai, 2020).
332
333 Considering the apparent flexibility of the gate, we sought to mutate the EMC4 interfaces
334 resolved in the cytoplasm versus the membrane. As described above, mutating residues that
335 together form a composite binding surface for the cytoplasmic domain of EMC4
336 (hEMC2$^{E146A+E149A+Q150A}$, hEMC2$^{E168A + D170A + K173A}$, **Figure 3F**), we observed a modest
337 accumulation of the tail-anchored insertase client (SQS) (**Figure 3G, Figure 3 – figure**
338 **supplement 1-2**). Likewise, mutating residues in the center of the gated cavity, close to one
339 of the unassigned helices in the closed gate conformation (hEMC3$^{V118A + I122A}$) (**Video 1,**
340 **Figure 5 – figure supplement 1**) led to an increase of SQS. This SQS accumulation effect
341 stands in contrast to mutating a residue that contacts the lumenal anchor of EMC4
342 (hEMC3^{F148L}), which caused a reduction of SQS levels (**Figure 5 – figure supplement 1**).
343
344 **The lipid-filled cavity is critical for both insertase-dependent and insertase-independent**
345 **EMC functions**
346
347 In addition to the gated cavity, the EMC harbors another membrane-accessible cavity. The
348 surface of the lipid-filled cavity includes contributions from EMC1, EMC3, EMC5 and
349 EMC6 (**Figure 6A**). In our structures the EMC2 N-terminus occludes cytoplasmic
350 accessibility to this cavity (**Figure 4D**, **Figure 6A-B**). However, this cavity may be accessible
351 from the membrane or the ER lumen. The respective distance from the cytoplasmic EMC2 N-
352 terminus to the lumenal side of the lipid-filled cavity is approximately 35 Å across, which is
353 close to the average ER membrane thickness (Mitra, 2004).

354
355 The lipid-filled cavity features a uniformly hydrophobic surface (**Figure 6C**) and
356 superimposes across our ensemble of EMC structures. As noted, we resolved several lipids in
357 our cryoEM maps lining the cavity wall and modeled four POPC (1-palmitoyl-2-oleoyl-sn-
358 glycero-3 phosphatidylcholine) molecules in the hEMC nanodisc map (**Figure 6C**). The
359 residues in close proximity to these lipids are moderately conserved (**Figure 6 – figure**
360 **supplement 1**). To characterize the functional role of the lipid-filled cavity, we mutated
361 cavity-lining and lipid-proximal residues (**Figure 6D, Figure 6 – figure supplement 2-3**).
362 Most of these mutations resulted in an increased abundance of the tail-anchored reporter
363 (SQS) and mild decrease in production of polytopic client reporters (B1AR, TMEM97).
364 However, one lipid-proximal mutant showed decreased levels of all three client reporter types
365 with varying severity (hEMC3^{R13E}) without altering overall EMC levels. An analogous
366 mutation in drosophila EMC3 was recently was reported to cause reduced levels of Rh1 in
367 this mutant background (Xiong, 2020). The amphipathic EMC1 brace helix, which packs
368 against the transmembrane helices of EMC5, is a structural hallmark of the lipid-filled cavity,
369 (**Figure 6D**). Here, mutating interfacial residues from EMC5 (EMC5$^{H19L+S23A+Q26L}$) caused a
370 marked decrease in the N-lumenal polytopic reporter (B1AR) and a mild decrease in the tail-
371 anchored client (SQS) with no effect on the TMEM97 reporter (**Figure 6F**). Unexpectedly,
372 mutating interfacial residues from EMC1 (EMC1$^{F437Y+R487K}$) showed a diametrically opposed
373 phenotype in which B1AR was unaffected, SQS accumulated and TMEM97 levels markedly
374 decreased (**Figure 6G**). Two other interfacial brace mutants which had yet different resulting
375 client flow cytometry profiles (**Figure 6 – figure supplement 3B-C**). The pleiotropic client
376 phenotypes across the panel of interfacial brace mutants suggest that this feature is critical for
377 multiple EMC functions.
378

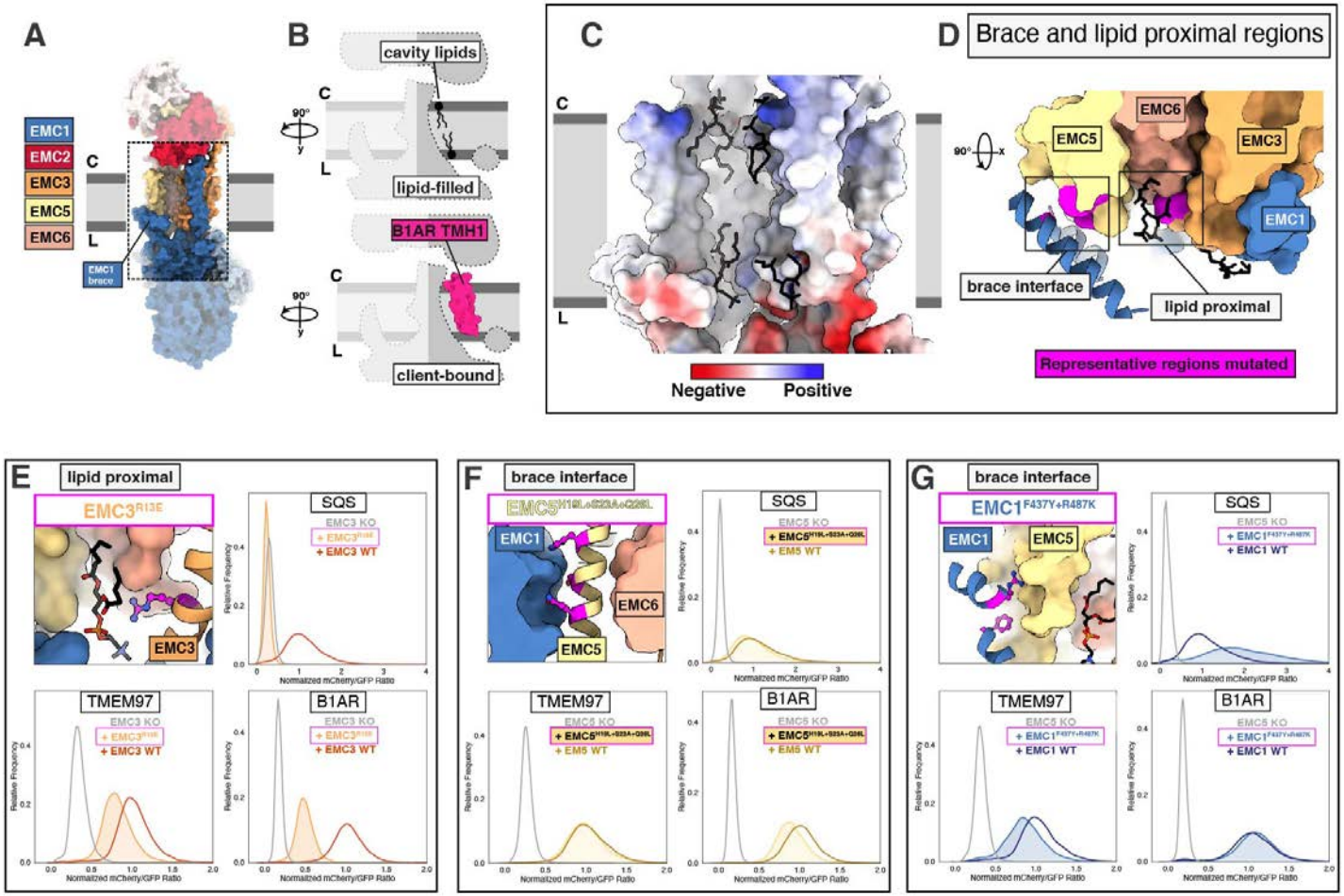

Figure 6: **A lipid-filled cavity in the EMC transmembrane domain stabilizes disparate client proteins.**

A) An EMC1 amphipathic brace helix delineates the boundary of the lipid-filled transmembrane cavity and packs against EMC5. Shown is a surface rendering of the hEMC model in nanodiscs. EMC4, EMC5, EMC6, and EMC1 subunits all contribute to the cavity lining.

B) The lipid-filled cavity in the hEMC nanodisc is occupied by several lipid molecules. Cartoon outlines of the gated cavity illustrate that the cavity could in principle allow for occupancy of a client helix (B1AR TMH1), possibly by lipid displacement or movement of the EMC1 brace helix.

C) The lipid-filled cavity has a uniform hydrophobic lining. Shown is an electrostatic surface rendering of the hEMC nanodisc structure colored as in Figure 5C. The cytoplasm-membrane interface contains positively charged residues and the lumenal interface contains negatively charged residues. Modeled phospholipid molecules are displayed in black.

D) Lipid-proximal and brace interface residues targeted for mutagenesis. Selected regions targeted for mutagenesis are colored in magenta and include brace interface mutations both in EMC1 and EMC5, as well as a lipid-proximal residue in EMC3.

E) Fluorescent client reporter stability assay for the hEMC3^{R13E} mutant, which is in close proximity to a modeled POPC molecule.

F) As in E) for the hEMC5$^{H19L+S23A+Q26L}$ mutant, which sits at the interface to the EMC1 amphipathic brace helix.

G) As in E) for the hEMC1$^{F437Y+R487K}$ mutant, which sits at the interface to the EMC5 transmembrane helices.

379 **The EMC lumenal domain is crucial for the biogenesis of multi-pass transmembrane**
380 **proteins**
381
382 Composed primarily of EMC1, EMC7 and EMC10, the extensive EMC lumenal domain
383 (**Figure 7A**) is important for polytopic client biogenesis and interactions with lumenal
384 chaperones (Luo, 2002; Shurtleff and Ithzak, 2018; Hiramatsu, 2019; Coehlo, 2019). EMC7
385 and EMC10 are scaffolded on two beta-propellers of EMC1, one distal and the other proximal
386 to the membrane. The lumenal cap differs between hEMC and yEMC, with a four-bladed
387 distal beta-propeller in yeast and eight-bladed distal propellor the human complex (**Figure**
388 **7B**). All three lumenal EMC subunits have structural folds known to participate in protein-
389 protein interactions (Reinisch & De Camilli, 2017). Mutations in this lumenal domain have
390 been linked to loss of the EMC complex (Bircham, 2011), a trafficking delay for membrane
391 protein Pma1 (Luo, 2002), and male infertility (Zhou, 2018).
392
393 Several regions of the lumenal domain form stabilizing interactions with the membrane
394 cavities. The gate helices of the gated cavity are anchored via the embedding of EMC4's C-
395 terminus within the membrane-proximal EMC1 propeller. The lipid-filled cavity is connected
396 to the ER lumenal domain via the amphipathic EMC1 brace helix, which is tethered to the
397 membrane-proximal EMC1 beta-propeller. The connections between the lumenal domain and
398 the transmembrane cavities could allow for conformational coupling during client handling.
399 Indeed, superimposing the two conformations presented above, the open and closed gate
400 states, revealed not only differences in the transmembrane domain but also a rotation of the
401 lumenal domain relative to the membrane cavities (**Video 2**). The lumenal positioning is
402 consistent for all three of our closed gate conformation reconstructions (hEMC detergent,
403 yEMC nanodisc, yEMC detergent). By contrast the one map with an open gated cavity
404 displayed a lumenal rotation and concomitant shifts in position of the EMC1 brace helix
405 (**Figure 7 – figure supplement 1**). Indeed, our set of interfacial EMC1 brace mutants
406 described above (**Figure 6F-G, Figure 6 – figure supplement 3**), showed differing client
407 phenotypes when mutated from either the EMC1 or the EMC5 side. This suggests a complex
408 conformational interplay between lumenal and transmembrane domains during the
409 engagement of diverse client types.
410
411 We investigated several known disease mutations in both conserved and human-specific
412 regions of EMC1 (**Figure 7C-E**, **Figure 7 – figure supplement 2-3)** (Harel, 2016; Abu-
413 Safieh, 2013; Amberger, 2019). One of these disease-associated residues sits near the anchor
414 point for the lumenal EMC4 transmembrane gate helix (hEMC1^{R881C}), while the majority are
415 found farther from the membrane (hEMC1^{G868R}, hEMC1^{A144T}, hEMC1^{T82M}) (**Figure 7C-E**).
416 Incorporating each of these disease mutations into our EMC functional assay resulted in lower
417 levels of the N-cytoplasmic polytopic client (TMEM97) and an increase in the level of the
418 tail-anchored client (SQS), discussed in more detail below.
419
420 Two different EMC1 mutants associated with cerebellar atrophy, visual impairment, and
421 psychomotor retardation (hEMC1^{T82M}, hEMC1^{G868R}), map to the hinge region between the
422 EMC1 beta propellers where EMC7 binds (**Figure 7D**). Both of these mutants, at this protein-
423 protein interface, result in depletion of the N-cytoplasmic polytopic client (TMEM97). EMC7

424 and EMC10 form beta-sandwich domains on either side of the membrane-proximal beta-
425 propeller of EMC1, and contact each other across the EMC1 surface. Consistent with our
426 structures, coupling of these subunits is supported by the prior finding that in the absence of
427 EMC7, EMC10 is also lost from the complex while the other EMC components appear
428 unaffected (Shurtleff and Ithzak, 2018). EMC7 and EMC10 have been proposed to be
429 auxiliary components with weaker phenotypes compared to core EMC subunits (Jonikas,
430 2009; Shurtleff and Ithzak, 2018; Dickinson, 2016). Upon deleting EMC7, multi-pass
431 transmembrane clients are retained in the ER but tail-anchored clients decrease in abundance
432 (Shurtleff and Ithzak, 2018).
433
434 Several features of our data suggest dynamic association of EMC7. Density for the EMC7
435 beta-sandwich at the hinge between the two EMC1 beta propellers was relatively weak in the
436 consensus hEMC nanodisc map (**Figure 2 – figure supplement 4**). Additional rounds of 3D
437 classification revealed two distinct classes, one with clear density for EMC7 and one with
438 weak density in this region. Mass spectrometric analysis of purified recombinant hEMC,
439 however, revealed that the abundance of EMC7 was similar to that of the other EMC
440 components (**Figure 1 – figure supplement 2; Supplementary file 1-2**). Both
441 reconstructions, with and without density for the EMC7 lumenal domain, displayed well-
442 resolved density for EMC10. Together, we conclude that EMC7 is associated with EMC1 in
443 two different conformational states of EMC7 with potentially distinct functions.
444
445 The OMIM database (Amberger, 2019) lists a mutation of unknown significance linked to
446 retinitis pigmentosa (hEMC1^{A144T}) residing in the EMC1 distal propeller (**Figure 7E**).
447 Additionally, we also generated mutations in two surface exposed patches of the membrane-
448 distal EMC1 beta-propeller projecting into the lumen (hEMC1^{R69D}, hEMC1^{G71S}, hEMC1$^{H93D +}$
449 $^{E138D + N282K}$, **Figure 7 – figure supplement 2-3**). Overall, these mutations displayed the same
450 client effect: a decrease in the N-cytoplasmic polytopic client reporter (TMEM97), no change
451 in the N-lumenal polytopic client reporter (B1AR), and accumulation of the tail-anchored
452 client reporter (SQS) (**Figure 7 – figure supplement 2-3**). Upon identifying antibodies
453 against yEMC we observed that the top two antibodies bind to a similar extended loop in the
454 distal yEMC1 beta-propeller, perhaps suggesting that this site is accessible for co-factor
455 binding in the ER. Intriguingly, this region of the lumenal domain corresponds to the region
456 where hEMC1 has an expanded distal beta-propeller. Taken together, the data provide
457 evidence that the lumenal domain is functionally coupled to the broader EMC role in
458 transmembrane client stabilization. Moreover, these data support that the EMC is acting as a
459 holdase chaperone to shield polytopic clients from degradation while they are folding to their
460 functional form.
461

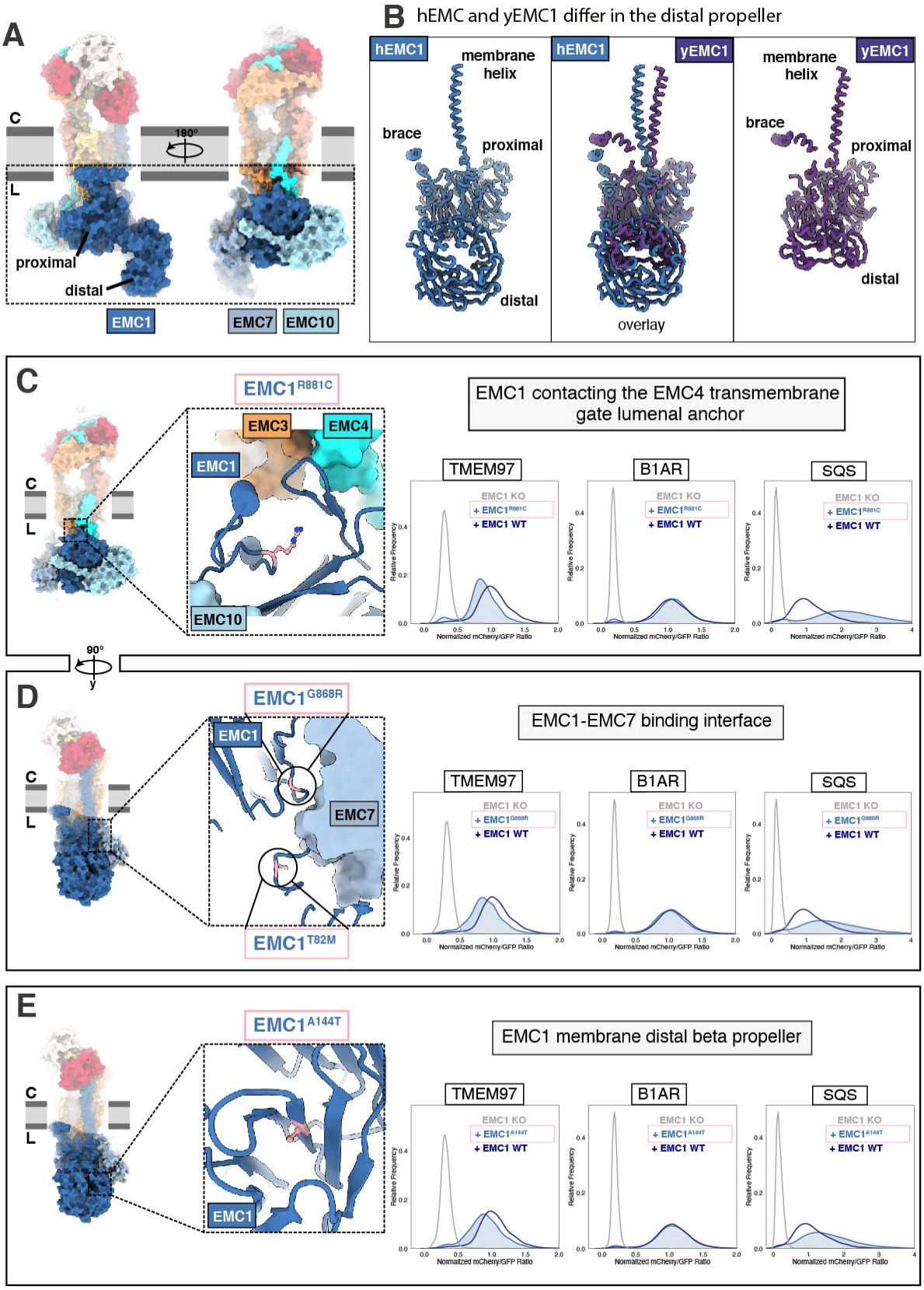

Figure 7: **The large EMC lumenal domain is the site for several annotated disease mutations.**

A) Two views of the hEMC nanodisc structure. Two beta propellers are present in EMC1, one proximal to the membrane and one distal.

B) EMC1 is the largest EMC subunit and differs in size between yeast and human. Shown are human EMC1 (nanodisc), an overlay of human and yeast EMC1 (both nanodisc), and yeast EMC1 (nanodisc).

C) The hEMC1^{R881C} mutant sits near the EMC4 lumenal gate anchor. Left: Location of the mutation (colored pink). Right: Fluorescent client reporter stability assay for hEMC1^{R881C}.

D) As in C) for the hEMC^{G868R} mutant.

E) As in C) for the hEMC^{A144T} mutant.

462 # Discussion
463
464
465 Our collection of yeast and human EMC structures revealed the intricate and dynamic
466 architecture of this multifunctional transmembrane molecular machine. The structures
467 served as the starting point for our systematic dissection of EMC's multifaceted functions
468 by exploring the impact of structure-based mutations on the ability of the EMC to support
469 the biogenesis of representative members of three classes of membrane proteins: SQS, a
470 tail-anchored protein, which exploits EMC's C-terminal insertase activity; B1AR, which
471 relies on EMC's N-terminal insertase activity; and TMEM97, a polytopic membrane
472 protein, which depends on the EMC for its biogenesis but does not rely on either of
473 EMC's terminal insertase activities. Our data revealed that a conserved dual membrane
474 cavity architecture supports the biogenesis of this diverse panel of transmembrane clients.
475
476 Overall, our studies present a nuanced picture of EMC's multifunctionality, revealing
477 structural regions that differentially impact production of the three distinct client types.
478 Unexpectedly, we also find that alterations to either the cytoplasmic or lumenal domain
479 of EMC lead to enhanced abundance of the TA substrate. Moreover, our work provides a
480 foundational framework for understanding how discrete yet allosterically coupled regions
481 of the complex enable the multiple functions of the EMC to support membrane protein
482 biogenesis. Taken together these studies suggest a model in which the EMC differentially
483 regulates the biogenesis of distinct membrane proteins, thereby contributing to cellular
484 coordination of membrane protein abundance in accordance with physiological needs.
485 We propose a model of the EMC functioning both as a terminal insertase as well as a
486 holdase chaperone that is potentially modulated by post-translational modifications, lipid
487 interactions, and protein-protein interactions [**FIGURE 8**].
488
489

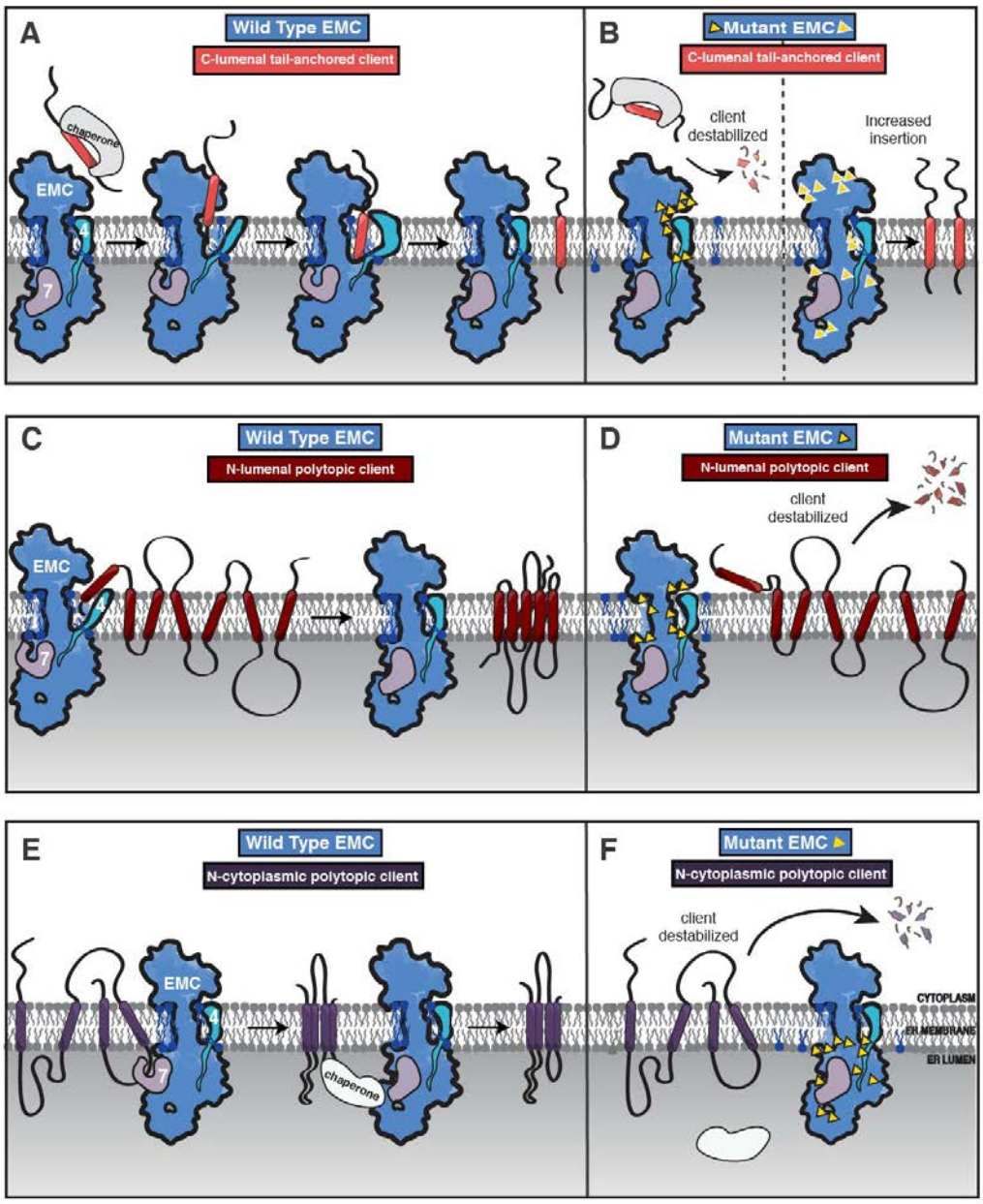

Figure 8: **Model of coordinated EMC functions**

A) Model of EMC insertase function for a C-lumenal tail anchored client. Cytosolic factors bring post-translationally localized clients to the ER. Then the client engages the EMC cytoplasmic domain. The polar roof modulates entry into the gated cavity. A hydrophobic slide facilitates the client helix fully entering the cavity. A lateral movement of the gate releases the client helix into the membrane and the EMC gate closes.

B) Our mutagenesis data provide the following insights into EMC regions of functional importance for each of the three client types we tested. Mutants are depicted by yellow triangles. Tail anchored client (coral) abundance was depleted upon mutagenesis of the cytoplasmic domain entrance to the gated cavity, polar and charged residues at the cytoplasm-membrane boundary, residues along the length of the gated cavity, in the hydrophobic seal to the lumen, and lipid interacting residues in both cavities (left). We also observed a subset of mutants that resulted in higher levels of the C-lumenal tail anchored client (right) that are positioned in the cytoplasmic domain cap, throughout the ER lumenal domain, and one mutation at the center of the gated cavity.

C) The EMC facilitates biogenesis of N-lumenal polytopic client protein B1AR (dark red).

D) Regions important for B1AR stability primarily map to the transmembrane region of the EMC structure, with depletion observed for lipid interacting residues on both sides of the cavity, the polar entrance roof of the gated cavity, and the EMC1 brace helix.

E) The EMC facilitates biogenesis of N-cytoplasmic polytopic client protein TMEM97 (dark purple).

F) Regions important for TMEM97 stability were primarily located in the lumenal domain spanning both propellers, in EMC1. In addition to these lumenal regions there was a depletion of TMEM97 at the lipid-interacting positions at the lumenal interface of both membrane cavities of the EMC.

490 ***Terminal insertase clients require an embedded insertase module within the EMC***
491
492 EMC3's fold at the interface between the cytoplasm and membrane forms the core of the
493 gated cavity and is reminiscent of proteins from the YidC family of insertases (Borowska,
494 2015; Dalbey, 2015; Anghel, 2017)**.** Indeed, mutations in either the cytoplasmic or
495 transmembrane domains of EMC3 establish that these features are critical for terminal
496 helix insertase activity. In light of our observation of multiple gate conformations, we
497 speculate that these conformations modulate insertion and release into the ER membrane.
498
499 Notably, mutating the surface of the cytoplasmic cap, which extends beyond the EMC3
500 cytoplasmic helices towards EMC8/9, resulted in an unexpected increase in C-tail anchor
501 client (SQS) abundance. Of the three clients analyzed, SQS was the only one to show
502 enhanced levels. It is unclear if this enhancement is SQS-specific or representative more
503 broadly of all post-translationally targeted EMC tail-anchored clients. Future studies will
504 be required to address if this is due to regulation of SQS by the EMC, parallel pathways
505 for inserting SQS into the membrane (i.e. mediated by TRC40/GET), and/or slower
506 cytoplasmic clearance of chaperone-bound SQS.
507
508 ***Both EMC cavities have resolved lipids and are critical for client biogenesis***
509
510 Both the N-terminal (B1AR) and C-terminal insertase (SQS) clients depend on the EMC
511 gated cavity. Indeed, both the SQS tail-anchored helix and the first transmembrane helix
512 of B1AR are moderately hydrophobic, with polar residues near the cytoplasmic end of
513 the transmembrane helix, and both showed a strong dependence on the gated cavity.
514 Nevertheless, our panel of mutants revealed some notable differences in the handling of
515 these two client types. B1AR showed more dependence than SQS on the lipid-filled
516 cavity in contrast to mutants elsewhere in the complex. One possible reason could be due
517 to differences in the mechanism of initial engagement: SQS is targeted to the ER by
518 cytoplasmic chaperones, while B1AR is targeted by SRP. Another key difference is that
519 B1AR is polytopic and needs to overcome the additional challenge of tertiary
520 transmembrane packing to reach its folded state. Future work will address the interplay
521 between B1AR synthesis and its co-translational engagement with the translocon versus
522 the EMC.
523
524 ***The EMC lumenal domain orchestrates holdase chaperone function important for***
525 ***polytopic clients***
526
527 Unlike the two terminal insertase clients we investigated, TMEM97 biogenesis was
528 negatively impacted by mutation of the lumenal EMC1. The depletion of TMEM97
529 observed in these mutant backgrounds is consistent with the lumenal domain contributing

530 to a holdase chaperone function, passively shielding its client while it is being
531 synthesized and/or folded (Zhang, 2017). Interestingly, the diametrically opposed
532 phenotype of mutants in the EMC lumenal domain on SQS raises the possibility that
533 occupancy by one type of client can support an EMC conformation that is unfavorable for
534 receiving the other. Alternative conformations could establish competition between client
535 types for EMC occupancy. One explanation for this observation is that there is a
536 conformational change between the insertase-active versus the holdase-active states.
537 Interestingly, we identified at least two EMC conformations in our collection of
538 structures, and EMC may adopt different conformations in various client and cofactor-
539 engaged states.
540
541 In yeast, the polytopic clients co-purifying with the EMC are also glycosylated. One
542 possible model is that the putative carbohydrate binding domains in EMC7 or EMC10
543 directly contribute to engagement with client proteins. We speculate post-translational
544 modifications on clients and the EMC could modulate function including client binding,
545 chaperone binding, or regulating signaling in response to cellular cues.
546
547 ***Potential role of the EMC as a master regulator of membrane protein biogenesis as the***
548 ***basis for its pleiotropic phenotypes***
549
550 Why does the cell use a multifunctional EMC molecular machinery rather than
551 specialized machinery for each of the functions encompassed by the EMC? Considering
552 that the cell already has general machinery (Sec61 translocon) and tail-anchor insertase
553 machinery (GET/TRC complex), we speculate that the EMC coordinates biogenesis of
554 diverse membrane proteins. Several observations suggest broader roles of the EMC as an
555 integrator of information sensing the protein and lipid environment and coordinating its
556 multiple activities, including the regulating the biogenesis of membrane proteins. For
557 example, the initial identification of the EMC included numerous genetic interactions
558 with both protein and lipid synthesis factors in yeast (Jonikas, 2009) and these disparate
559 interdependencies have been subsequently observed in numerous species including
560 human EMC (Lahiri, 2014; Tang, 2017; Guna, 2018; Volkmar, 2019; Volkmar, 2020).
561 Also, several client proteins are enzymes or cofactors involved in multiple stages of lipid
562 synthesis or trafficking, and this may provide a unifying explanation for the range of
563 genetic interactions and co-essentiality observations reported to date (Guna, 2018;
564 Shurtleff and Ithzak, 2018; Volkmar, 2018; Tian, 2019; Wainberg, 2019; Corradi, 2019;
565 Volkmar, 2020). In this regard, one structural feature of particular interest is the EMC1
566 amphipathic brace, which resides adjacent to the lipid-filled cavity. This conserved
567 feature sits within the interfacial membrane boundary, raising the possibility that it can
568 modulate the lipid or protein composition of this cavity. Notably, several other membrane
569 proteins involved in ER homeostasis, including Opi1 and Ire1, also contain amphipathic
570 helices that have been proposed to sense the properties of the lipid bilayer (Volmer, 2013;
571 Jacquemyn, 2017; Halbleib, 2017; Hofbauer, 2018; Cho, 2019). Future work will explore
572 how the EMC overall, and the EMC1 brace helix in particular, govern client release into
573 the membrane, interface with the local structure of the lipid bilayer, and play roles in
574 specific client-lipid interactions.
575

576 In addition to the three client classes we investigate here, it is clear that EMC has a
577 broader range of clients including multi-protein assemblies (Richard, 2013; Talbot,
578 2019), lipid modulating proteins (Volkmar, 2018), lipid binding proteins (Salas-Estrada,
579 2018; Sejdju, 2020), and those with helices that do not span the bilayer (Lin, 2019; Ngo,
580 2019). The compartmentalization and interdependence that we observe for effects of
581 mutations on client handling provide a foundation for understanding this
582 multifunctionality. We propose that the complexity of the EMC machine, combining
583 insertase and holdase chaperone functions within one molecular machine, has arisen to
584 mitigate the error prone biogenesis of a diverse range of membrane spanning proteins in
585 the dynamic environment of the ER.
586

587 # Materials and Methods

588

589 Reagents used for experiments described and reagents made as part of this study are
590 listed in Supplementary Table 2.

591 **Cell Line Maintenance**

592 K562 dCas9 KRAB cells were grown in RPMI 1640 (GIBCO) with 25 mM HEPES,
593 2 mM l-glutamine, 2 g/L $NaHCO_3$ and supplemented with 10% (v/v) fetal bovine serum
594 (FBS), 100 units/mL penicillin, 100 µg/mL streptomycin, 2 mM l-glutamine. HEK293T
595 cells were grown in Dulbecco's modified eagle medium (DMEM, GIBCO) with
596 25 mM d-glucose, 3.7 g/L $NaHCO_3$, 4 mM l-glutamine and supplemented with 10% (v/v)
597 FBS, 100 units/mL penicillin, 100 µg/mL streptomycin. All cell lines were grown at
598 37°C. All cell lines were periodically tested for Mycoplasma contamination using the
599 MycoAlert Plus Mycoplasma detection kit (Lonza).

600 **DNA transfections and virus production**

601 Lentivirus was generated by transfecting HEK39T cells with standard 4th generation
602 packaging vectors using TransIT-LT1 Transfection Reagent (Mirus Bio). Media was
603 changed 10 hours post-transfection. Viral supernatant was harvested 60 hours after
604 transfection, filtered through 0.45 µm PVDF filters and frozen prior to transduction.

605 **Knockout EMC Cell Lines**

606 A single and dual knockout guide system was developed in the pX458 backbone
607 (Addgene plasmid # 48138) with guides targeting EMC1, EMC2, EMC3, or EMC5 (see
608 reagents table). Targeting guides were selected using the Broad's guide selection tool
609 (https://portals.broadinstitute.org/gpp/public/analysis-tools/sgrna-design). For the single
610 EMC5 knockout system, an EMC5 targeting guide was cloned into pX458 by digesting
611 with BbsI and ligating to annealed oligos for the EMC5 sgRNA. For the dual knockout
612 system, a four-step cloning process generated the final knockout plasmid: 1) Each of the
613 two guides targeting the same locus were individually cloned into pX458. 2) Then
614 pX458_sgRNA1 was digested with XbaI 3) SgRNA2 cassette from pX458_sgRNA2 was

615 PCR amplified with oligos containing overhangs spanning the XbaI cloning site and
616 purified. 4) Finally, the final dual guide vector was generated by Gibson cloning
617 (NEBuilder).
618
619 To generate the EMC knockout cell lines, K562 dCas9 KRAB cells were nucleofected
620 with the respective EMC knockout plasmids using Lonza SF Cell Line 96-well
621 Nucleofector™ Kit (V4SC-2096). Two days post nucleofection, GFP-positive cells were
622 single cell sorted into 96-well plates using BD FACS AriaII. After colonies from single
623 cells grew out, genomic DNA was isolated using QuickExtract (Lucigen), the sgRNA-
624 targeted sites were PCR amplified and then NGS-sequenced via Genewiz's EZ-Amplicon
625 service. Sequencing data was analyzed and aligned to the respective reference alleles in
626 the human genome. Clones whose alleles harbored only indel mutations for EMC1,
627 EMC2, EMC3, and EMC5 (full knockouts) respectively were further validated on the
628 protein level.
629
630 **Dual fluorescent EMC client reporter cell lines**

631 Dual client reporters for TMEM97, ADRB1, and SQS were introduced lentivirally into
632 each of the EMC1, EMC2, EMC3, and EMC5 knockout cell lines. Three days post-
633 transduction, GFP/mCherry positive cells were sorted on BDAriaII.

634

635 **Mutant EMC cell lines**

636 The EMC mutant genes were synthesized and cloned by Twist into pKDP119-SFFV-
637 [insert site]-IRES-Puro-P2A-BFP. For EMC subunit mutation details refer to the reagents
638 table. Mutant EMC cell lines were generated by lentiviral introduction of the respective
639 EMC mutant subunit into the respective knockout cell lines (EMC1, EMC2, EMC3 or
640 EMC5) containing the dual fluorescent reporters for each EMC client
641 (pKDP110_ADRB1_mCherry_P2A_GFP, pKDP111_TMEM97_mCherry_P2A_GFP, or
642 GFP_P2A_mCherry_FDFT1_TMD_opsintag). The expression of each fluorescent
643 reporter was read out 6 days after puromycin selection in each of the EMC mutant cell
644 lines.
645

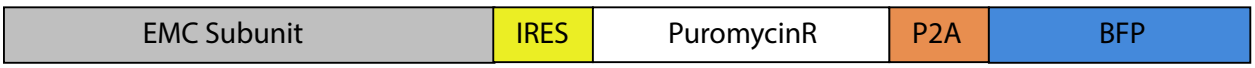

646
647
648 **Flow analysis**

649
650 For each EMC mutant cell line, 20 000 live cells were recorded on Attune NxT flow
651 cytometer. FlowCal flow analysis package was used for analysis in Python. First, live
652 cells were gated based on FSC/SSC. Then GFP (BL1-A) and mChery (YL2-A) were
653 plotted for each mutant and control cell line. mCherry:GFP intensity ratios were
654 calculated for individual cells in each cell line. Fluorescence ratios for each substrate in
655 an EMC mutant cell line were normalized to the mCherry:GFP ratio of the same substrate
656 in the EMC wild type rescue cell line. Distributions of fluorescence ratios were plotted as
657 histograms in Python using seaborn.
658
659 **Western Blotting**
660
661 Cell pellets were lysed using lysis buffer (20 mM Tris pH 7.5, 150 mM NaCl, 5 $MgCl_2$,
662 1% Triton x-100, 1 mM DTT, 24 U/ml Turbo DNase (Ambion). Clarified lysate was
663 quantified and samples were boiled with 4x LDS sample (Thermo Fisher, NP0007) buffer
664 for 5 mins at 95C. Samples were separated on 4-12% or 12% Bolt Bis-Tris Plus Gels
665 (Invitrogen, NP0322PK2). Proteins were transferred onto nitrocellulose membranes using
666 Bio-Rad Trans-Blot Turbo transfer system. Membranes were blocked in Odyssey
667 Blocking Buffer (LI-COR, 927-50000) for an hour at room temperature. Blocked
668 membranes were incubated with primary antibody diluted in TBST and incubated
669 overnight at 4C on a shaker. Primary antibodies were detected by incubating membranes
670 with 1:10000 dilution of IRDye-conjugated (LI-COR) secondary anti-mouse and anti-
671 rabbit antibodies for 1 hour at room temperature. Blots were visualized using LI-COR
672 imaging system. The primary antibodies used in this study are in the reagents table.
673
674 **Yeast strains**
675
676 Strain BY4741 and BY4742 were used as the wild-type parental strains for the creation
677 of the yEMC overexpression strain. Yeast homologous recombination (Rothstein, 1991)
678 was used to generate yeast strains. For the overexpression strain, the endogenous
679 promotor for each yEMC subunit (yEMC1, yEMC2, yEMC3, yEMC4, yEMC5, yEMC6,
680 yEMC7, yEMC10) were replaced with a TEF2 promoter. In addition, EMC5 was tagged
681 at the C-terminus with linker-TEV-linker-3xFlag. Auxotrophic markers and drug
682 selection markers in both BY4741 and BY4742 were employed to add this promoter
683 modification to all of these eight subunits and the two strains were crossed to create the
684 resulting BY4743 strain used for immunoprecipitation. Endogenous EMC yeast strain
685 was made using W303a wild type parental background (leu2-3,-112; his3-11,-15; trp1-1;
686 ura3-1; ade2-1; can1-100; MATa). Homologous recombination was used to integrate a
687 linker-TEV-linker-3xFlag at the C-terminus of EMC coding sequence. Genomic PCR
688 was conducted to verify integration.
689
690 **Design and purification of fragments antigen binding (Fab) DH4 and DE4**
691
692 Fabs were identified as described in these studies (Kim, 2011; Wu, 2012). Overexpressed
693 yEMC solubilized in DDM as described above was biotinylated and streptavidin
694 magnetic beads were used to capture yEMC, which was then subjected to a Fab phage

695 library. Unbound Fabs were washed away and then binding Fabs were eluted and
696 analyzed by ELISA. Two Fabs were identified binding EMC, Fab DH4 and DE4.
697
698 **Purification of DH4 and DE4 Fabs**
699
700 Plasmid with either Fab DH4 or DE4 were transformed into BL21 Gold Star cells and
701 plated onto agarose plates with 2x YT + 2% glucose + Ampicillin. Cultures were
702 inoculated from resulting colonies for overnight growth at 30 °C into 2xYT + 2% glucose
703 + Amp. In the morning dilute overnight culture to OD_{600} of 0.05 in 1L, in a 2.8 L flask of
704 2xYT + 0.1% glucose + Amp. Grow the culture at 180 rpm at 37 °C shaker until OD_{600} of
705 0.6, then, switch to shaking at 19 °C for 1 hour. Next, induce with 0.4 mM IPTG. Shake
706 at 180 rpm at 19 °C for 18-20 hours. Spin 1L cultures down at 3500 rpm in large
707 Beckman Centrifuge at 4 °C for 20 minutes in (8.1 rotor). Discard media and gently
708 resuspend cell pellet in ice-cold 20 ml in Buffer 1 (0.2 M Tris pH 8.0, 0.5 mM EDTA, 0.5
709 M Sucrose) on ice. Transfer the resuspended cells from step 2 into 2 smaller JLA 25.5
710 centrifuge tubes. Add 20 ml of ice cold ddH_2O with 2x protease inhibitor cocktail (Roche
711 Complete Ultra, Millipore Sigma 5056489001) from step 3 to the resuspended pellets.
712 Incubate at on ice for one hour occasionally swirling samples gently. Spin periplasmic
713 fractions at 13,000 x g for 15 min, 4 °C, rotor 25.50. Wash 500uL Ni resin (Qiagen, Ni-
714 NTA, 30210) per periplasmic fraction four times in Buffer 2 (50 mM Tris pH 8.0, 250
715 mM NaCl). Add $MgCl_2$ and imidazole to a final concentration of 10 mM to each
716 periplasmic fraction. Add beads to periplasmic fractions and nutate at 4 °C for 2
717 hours. Spin down beads at 2000 x g, 10 minutes, 4 °C. Transfer beads either to a 50 mL
718 gravity column. Wash the beads with 20 column volumes of Buffer 3 (50 mM Tris pH
719 8.0, 500 mM NaCl, 20 mM Imidazole). Elute protein with 3 column volumes of Buffer 4
720 (50 mM Tris pH 8.0, 500 mM NaCl, 300 mM Imidazole). Analyze eluate by SDS-PAGE
721 4-12% Invitrogen (Invitrogen, NP0321PK2). Fabs as two bands run around 30 kDa in
722 reducing conditions, or 50 kDa in non-reducing conditions. Dialyze eluate O/N in
723 Dialysis cassette 10 kD molecular weight cutoff at 4 °C against 150 mM KOAc, 20 mM
724 HEPES pH 6.8.
725
726 **Purification of overexpressed yeast EMC5-3xflag**
727
728 The OE-Emc5-3xflag yeast strain were grown in YEPD media in a 40 L fermenter,
729 harvested and flash frozen in liquid nitrogen. Cell pellets were thawed and diluted in lysis
730 buffer (50 mM HEPES pH 6.8, 150 mM KOAc, 2 mM MgOAc, 1 mM CaCl2, 0.2M
731 Sorbital, 2x Protease Inhibitor). Bead beating (10 times → 1 minute on, 2 minutes off)
732 was used to lyse cells. For 25g of cells, 0.1 mm cold beads were added and lysis buffer
733 up to the top of the 50 mL canister. After lysis, beads were filtered and solution
734 centrifuged at 10,000 xg for 10 minutes. Supernatants were ultracentrifuged at 42,000
735 RPM (Ti 45 rotor) for 2 hours. Supernatant was discarded. Membrane pellet was
736 combined with the lipid layer, and resuspended in lysis buffer and then a precooled
737 dounce homogenizer was used to dounce 20 times. Membranes were aliquoted and flash
738 frozen in liquid nitrogen. On ice, 150 mL of solubilization buffer (50 mM HEPES pH
739 6.8, 150 mM KOAc, 2 mM MgOAc, 1 mM CaCl2, 15% glycerol, 1% b-DDM, 2x
740 Protease Inhibitor) was added incrementally to 7.5g of thawing membranes, nutated at

741 4°C for 1 hour in JA 25.5 rotor tubes, and centrifuged at 20,000 rpm for 45 minutes.
742 Meanwhile 2.5 mL of αFLAG agarose beads (Millipore A2220) were rinsed in 50mL of
743 low salt buffer (50 mM HEPES pH 6.8, 150 mM KOAc). Supernatant was added to
744 αFLAG beads and nutated at 4°C for 2 hours. Resulting solution was applied over a glass
745 column. After flowing through unbound solution, αFLAG beads were washed with 100
746 mL low salt buffer, 100 mL high salt buffer (50 mM HEPES pH 6.8, 300 mM KOAc,
747 0.05% b-DDM), and 100 mL low salt buffer. αFLAG beads were resuspended in 10 mL
748 of low salt buffer and 300 uL of TEV (1.15mg/mL) was added and nutated overnight at
749 4°C. Removed supernatant from beads by low speed spin and applied over 500 uL of
750 NiNTA beads equilibrated with low salt buffer to remove excess TEV. Flow through
751 glass column and collect supernatant. Using a 100 kD concentrator (Millipore,
752 UFC910008) solution was concentrated to 2mg/mL. Concentrated EMC protein was
753 applied to the Akta Explorer Superose 6 Increase column (Cytiva, 29091596) for size
754 exclusion chromatography in the size exclusion buffer (20 mM HEPES pH 6.8, 150 mM
755 KOAc, 0.05% b-DDM). Fractions were evaluated by SDS-PAGE Coomassie stain and
756 negative stain electron microscopy then EMC peak fractions were pooled and incubated
757 with 2x molar excess of Fab, either Fab DH4 or Fab DE4, for 30 minutes on ice. Solution
758 was applied to Akta Explorer Superose 6 Increase for size exclusion of Fab bound EMC.
759 Resulting EMC-Fab fractions were evaluated by SDS-PAGE Coomassie stain and EMC-
760 Fab peak fractions were pooled.
761
762 **Purification and nanodisc reconstitution of endogenous yeast EMC5-3xflag**
763
764 Yeast was grown in rich media (YPAD) in a 65L fermenter until OD 2.6. Cell pellets
765 were harvested and flash frozen in liquid nitrogen. Pellets were ground using three cycles
766 in a French press. As above, the resulting solution was ultracentrifuged to separate
767 membranes, dounced to homogenize, and flash frozen in liquid nitrogen. Thawed
768 membranes were solubilized in 1% b-DDM (Anatrace, D310) nutating at 4°C for 1 hour
769 then centrifuged to separate solubilized membranes from the pellet. Supernatant was
770 applied to equilibrated αFLAG beads, nutated at 4°C for 1 hour, and applied over a
771 disposable plastic column at 4°C. αFLAG beads were washed with low salt buffer and
772 high salt buffer. Then washed with low salt buffer with b-DDM+CHS (Anatrace, CH210)
773 (10:1) in place of b-DDM. αFLAG beads were then transferred to a 15 mL Eppendorf
774 tube for TEC cleavage and nanodisc reconstitution.
775
776 Bio-Beads SM-2 (Bio-Rad) were prepared ~400 uL biobeads, rinsing with EtOH, and
777 then water four times. Yeast Extract Total (Avanti Polar Lipids, 190000C-100mg) was
778 prepared by transferring chloroform resuspended solution to a glass vial, drying the lipids
779 into a film with nitrogen gas, drying in a vacuum desiccator overnight, and then
780 solubilizing the lipids first in water and then in size exclusion buffer with DDM+CHS by
781 bath sonication, aliquots stored at -20 °C until use. 200 uL of TEV protease (5 mg/mL)
782 and 150 uL of 1mg/mL Yeast Total Extract solubilized in b-DDM+CHS, at room
783 temperature for 30 minutes. Then added MSP1D1, purified as described previously
784 (Ritchie, 2009), to a ratio of 200:10:1 (Yeast total extract:MSP1D1:EMC), at 4°C for 10
785 minutes. Then activated Bio-Beads SM-2 (Bio-Rad), ~300 uL, were added and nutated
786 overnight. On-bead reconstitution employed adapted from (Laverty, 2019). In the

787 morning ~100 uL more Bio-Beads SM-2 (Bio-Rad) were added and 2x molar excess of
788 FabDH4, nutated for another hour. Beads and solution applied to an EconoPac column
789 (Bio-Rad). Flow through was collected and solution was applied to a 100 kD (Amicon)
790 concentrator. Resulting concentrated EMC was applied to the Akta Explorer Superose 6
791 Increase column for size exclusion chromatography. Peak fractions were pooled for SDS-
792 PAGE Coomassie stain, negative stain, and cryo electron microscopy evaluation.
793
794 **Cryo-EM Sample Preparation and Data Collection for yEMC**
795 Overexpressed EMC + Fab DE4 in b-DDM
796 Following size exclusion sample was prepared for cryo electron microscopy. 3 µL of
797 sample (0.1mg/mL EMC + Fab DE4 in 20mM HEPES pH 6.8, 150 mM KOAc, 0.05% b-
798 DDM) was applied to the grid, incubated for 10 seconds, then blotted with no offset for
799 6.5 seconds and plunge frozen in liquid ethane using a Vitrobot Mark III at 5° C,
800 Whatman #1 filter paper, and 100% humidity. Protein was frozen on glow discharged
801 Ultrathin Carbon Film on a Lacey Carbon Support Film (Ted Pella, 01824) and stored
802 under liquid nitrogen until imaging. This dataset was collected on the 300 kV Technai
803 Polara at UCSF with a 30 µm C2 aperture, 100 µm Objective aperture, and K2 Summit
804 detector operated in super-resolution mode. 1536 micrographs were collected using
805 SerialEM (Mastronarde, 2005) at a magnification of 31,000X (0.6078 Å/ super resolution
806 pixel) as dose-fractionated stacks of 40 frames x 0.2 second exposures (1.42 $e^-/Å^2$) for a
807 total dose of ~56.85 $e^-/Å^2$ (see Table S1).
808
809 Overexpressed EMC + Fab DH4 in b-DDM
810 Following size exclusion sample was prepared for cryo electron microscopy. 3 µL of
811 sample (0.1mg/mL EMC + Fab DH4 in 20mM HEPES pH 6.8, 150 mM KOAc, 0.05% b-
812 DDM) was applied to the grid, incubated for 10 seconds, then blotted with no offset for 7
813 seconds and plunge frozen in liquid ethane using a Vitrobot Mark III at 4° C, Whatman
814 #1 filter paper, and 100% humidity. Protein was frozen on glow discharged Ultrathin
815 Carbon Film on a Lacey Carbon Support Film (Ted Pella 01824). This dataset was
816 collected at the HHMI Janelia Research Campus on Titan Krios 2, a 300 kV microscope
817 equipped with a 50 µm C2 aperture, 70 µm objective aperture, and K2 Summit detector
818 operated in super-resolution mode. 3357 micrographs were collected using automated
819 SerialEM (Mastronarde, 2005) collection with defocus range set between -1 and -3 µm at
820 a magnification of 22,500X (0.655 Å/ super resolution pixel) as dose-fractionated stacks
821 of 50 frames x 0.2 second exposures (1.165 $e^-/Å^2$) for a total dose of ~58.3 $e^-/Å^2$ (see
822 Table S1).
823
824 Endogenous EMC + Fab DH4 in MSP1D1-Yeast Total Extract nanodisc
825 Following size exclusion sample was prepared for cryo electron microscopy. 4 µL of
826 sample (~0.8mg/mL EMC + Fab DH4 in nanodisc in 20mM HEPES pH 6.8, 150 mM
827 KOAc, 0.05% b-DDM) was applied to the grid from the left side, then blotted with no
828 offset for 2.5 seconds, then another 4 uL of sample was applied to the right side of the
829 grid (without glow discharge) and blotted for 3.5 seconds, and plunge frozen in liquid
830 ethane using a Vitrobot Mark IV at 4° C, Whatman #1 filter paper, and 100% humidity.
831 Protein was frozen on R 1.2/1.3 grids with 300 Au mesh (Quantifoil, Germany). This
832 dataset was collected at UCSF on the Titan Krios 2, a 300 kV microscope equipped with

833 a 70 µm C2 aperture, 100 µm objective aperture, and K3 detector operated in CDS mode.
834 5949 micrographs were collected using automated SerialEM (Mastronarde, 2005)
835 collection with defocus range set between -0.8 and -2 µm at a magnification of 105X
836 (0.4265 Å/ super resolution pixel) as dose-fractionated stacks of 100 frames x 0.06
837 second exposures (0.67 $e^-/Å^2$) for a total dose of ~67 $e^-/Å^2$ (see Table S1).
838
839 **Image Analysis and 3D Reconstruction for yEMC**
840 Overexpressed EMC + Fab in b-DDM
841 Image processing schematic (**Figure 2 – Figure Supplement 1**) and Supplementary
842 Table 1 have additional details. All dose-fractionated image stacks were corrected for
843 motion artefacts, 2x binned in the Fourier domain, and dose-weighted using MotionCor
844 (Li, 2013) for the DDM datasets, resulting in one dose-weighted and one unweighted
845 integrated image per stack with pixel sizes of 1.22Å (DDM - Polara) or 1.31Å (DDM –
846 Janelia Krios). The parameters of the Contrast Transfer Function (CTF) were estimated
847 using GCTF-v1.06 (Zhang, 2016) and the motion-corrected but unweighted images. For
848 each dataset ~1000 particles per dataset were manually selected and averaged in 2D using
849 RELION 2.0 (Kimanius, 2016). The resulting class sums were then used as templates for
850 automated particle picking using Gautomatch-v0.55 (Zhang, 2016), followed by
851 extraction in RELION 2.0. Five rounds of 2D classification were performed to eliminate
852 ice contamination, particles near carbon edges, and 2D class without visible secondary
853 structure features. Subsequent particles were subjected to 3D auto-refine in Relion 2.0.
854 The Polara dataset was processed providing a reference model created in Spider (Shaikh,
855 2008) roughly mimicking the dimensions seen in 2D projections, then a second round
856 was run using the resulting volume before two rounds of 3D classification without
857 alignments. The resulting subset of particles were subjected to 3D auto-refine and then
858 3D classification with local alignments. The best 83,599 particles were then subjected to
859 3D refinement resulting in a 3D volume with ~8 Å reported resolution, which was
860 rescaled and low-pass filtered for use as the reference for the DDM Krios dataset. 3D
861 classification without alignments, 3D refinement, 3D classification with local alignments,
862 and 3D auto refinement were performed resulting in a ~7 Å structure composed of
863 170,186 particles. Both resulting reconstructions overlay with one another, despite having
864 Fab DH4 in one sample and DE4 in the other. Furthermore, they both displayed a severe
865 orientation bias, and 3D reconstructions appeared streaky.
866
867 Particles from both datasets were re-extracted and scaled to a common pixel size of 1.35
868 Å and box size of 266. The combined dataset was subjected to two rounds of 3D
869 refinement to form a consensus structure at ~6.8 Å all conducted in Relion 2.0. These
870 particles were then subjected to 3D refinement in THUNDER (Hu, 2018) using soft-
871 edged mask. THUNDER produced a resulting 3D reconstruction that visually appeared
872 less distorted along the axis of overrepresented views and resulted in a ~4.8 Å consensus
873 structure. Postprocessing was done in Relion 3.0 resulting in a ~4.3 Å sharpened map and
874 output was used to generate the FSC plot (**Figure 2 – figure supplement 1**). Molecular
875 graphics and analyses were performed with the UCSF Chimera package (Pettersen, 2004)
876 and Coot 0.8.7 and Coot 0.9 (Emsley, 2004; Emsley, 2010). Local resolution was
877 computed by inputting mask and half maps into Cryosparc 2 local resolution (Stagg,

2014; Punjani, 2017; Punjani, 2019) and visualizing the resulting map and scaling in UCSF Chimera.

Endogenous EMC + Fab DH4 in MSP1D1-Yeast Total Extract nanodisc

All dose-fractionated image stacks were corrected for motion artefacts, 2x binned in the Fourier domain, and dose-weighted using MotionCor2 (Zheng, 2017) using Focus (Biyani, 2017) resulting in a 2x binned pixel size of 0.835Å (nanodisc – UCSF Krios). The parameters of the Contrast Transfer Function (CTF) were estimated using GCTF-v1.06 (Zhang, 2016) and the motion-corrected but unweighted images. Data were then split into five groups of 1000 micrographs for processing until they were combined in 3D. Roughly ~1000 particles per subset were manually selected and averaged in 2D using RELION 3.0 (Zivanov, 2018) for the nanodisc dataset. The resulting class sums were then used as templates for automated particle picking using Autopick in Relion 3.0, followed by extraction and one round of 2D classification per subset to remove ice contamination. The resulting subsets of particles were subject to 3D refinement. Combining the RELION star files these particles were imported into Cryosparc 2.0 (Punjani, 2017; Punjani, 2019) along with a reference model. These data were subjected to non-uniform homogenous refinement, a round of four class 3D heterogeneous refinement, another round of non-uniform refinement for the best class (roughly 1.2 million particles), non-uniform homogeneous refinement, a round of two class 3D heterogeneous refinement, and another non-uniform homogeneous refinement for the best class (roughly 500,000 particles). These were then exported to RELION 3.0 using PyEM (Asarnow, 2019). 3D Classification was performed with local alignments, then CTF refinement of the best class (230,528 particles) resulting in a ~3.2 Å final reconstruction. This was post-processed in both RELION 3.0 and using phenix.autosharpen, both resulting maps were used for model building.

Model building and refinement of yEMC in nanodiscs

Structural biology applications used in this project were compiled and configured by SBGrid (Morin, 2013). The yeast EMC structure was built de novo using Coot (**version 0.8.7 and 0.9**) and UCSF ChimeraX (Goddard, 2018). Visible secondary structure was built by hand for the entire structure using overlays of the yEMC detergent consensus map as well as the yEMC nanodisc unsharpened and sharpened map. Starting with the best resolved transmembrane helices, sequence was placed for each of the predicted transmembrane helices, using TMHMM (Krogh, 2001), in the yEMC proteins. Visual inspection for landmark residues (tryptophan, tyrosine, leucine, and proline) in the sequences that correlated with the position of well densities as well as fit correlation in UCSF Chimera was computed to assign identities for yEMC1, yEMC3, yEMC5, and yEMC6. Connectivity between the EMC1 assigned helix to the lumenal domain was used to start assigning sequence for the lumenal portion of EMC1. Secondary structure prediction was computed for all yEMC proteins using Phyre2 (Kelley, 2015) and Quick2D, a tool within the Max-Plank Institute for Developmental Biology Bioinformatics Toolkit that visualizes several different secondary structure predictors (Jones, 1999; Cuff and Barton, 1999; Ouali and King, 2000; Rost, 2001; Lupas, 1991; Jones, 1994; Ward, 2004; Peng, 2006; Obradovic, 2005). Secondary structure prediction was used to check and guide sequence assignment of beta strands and helices. Next

924 several homology models were computed and overlain for yEMC2, with a predicted TPR
925 structural domain, using Robetta (Raman, 2009; Song, 2013), I-TASSER (Zhang, 2008;
926 Roy, 2010; Yang, 2015), Phyre2 (Kelley, 2015), and RaptorX (Kallberg, 2012). These
927 were used in addition to secondary structure prediction to guide sequence assignment,
928 loop building, and helical packing. Fab DH4 starting structure was computed using
929 Phyre2 1-to-1 threading against a crystal structure of a monoclonal Fab (PDB 1M71,
930 Vyas, 2002). EMC3, EMC5, and EMC6 were built off of the transmembrane helices
931 using sphere refinement, real space refinement, regularization, and visual monitoring of
932 the Ramachandran plot in Coot. EMC7 and EMC10 both form beta sandwich folds on the
933 exterior of the EMC1 lumenal domain, beta strand sequence was placed for both in both
934 densities, position of aromatic residues and loop length differed between the two
935 allowing assignment of each. After building EMC1-3, EMC5-7, and EMC10, there
936 remained several transmembrane helices and a beta strand fitted into the lumen but not
937 connected to EMC1, EMC7, or EMC10. The resolution of the lumenal domain is better
938 than 3 Å in most parts allowing for sequence placement of the EMC4 C-terminus and
939 C-terminal transmembrane helix. The connectivity of the transmembrane helix to
940 the cytoplasmic domain was not resolved. However, there was an additional poorly
941 resolved short helix and loop density in the cytoplasmic domain which was assigned
942 to EMC4.
943
944 Two poorly resolved transmembrane helices remained, however due to the fact they
945 did not have clear connectivity to any built strand, poly alanine alpha helices were
946 built in but not assigned to a yEMC protein (**Figure 5 – figure supplement 3**). EMC4
947 had density in the cytoplasmic domain as well as the lumenal domain, suggesting
948 that it has either one or three transmembrane passes. EMC7 and EMC10 were
949 predicted to have transmembrane helices however the connection between the
950 lumenal densities and those predicted transmembrane helices was not clear.
951 Additional density that was not built into was visualized in UCSF ChimeraX (Goddard,
952 2018) and allowed for subsequent assignment of several glycosylated residues and one
953 POPC molecule. Each subunit was built in a separate pdb file and subjected to iterative
954 rounds of phenix.real_space_refine (Adams, 2011; Liebschner, 2019) into segmented
955 maps preceded and followed by adjustment in Coot. Manual assignment of secondary
956 structure restraints was used and improved during Phenix refinement. Once all of the well
957 resolved secondary structure was assigned to yEMC subunits, PDBs were combined and
958 subjected to iterative rounds of phenix.real_space_refine (Adams, 2011; Afonine, 2018;
959 Liebschner, 2019) in the unsharpened and then sharpened maps. Loops were built back
960 where the connectivity was clear and then refined again in Phenix and Coot. PDBs were
961 prepared for refinement steps using phenix.reduce to add hydrogens throughout
962 refinement steps, ReadySet to generate cif restraints, and Phenix PDB preparation tool for
963 creating mmCIF files for deposition. Representative regions of the model as well as the
964 map-to-model FSC can be found in **Figure 2 – Figure Supplement 5**.
965

966 **Cryo-EM sample preparation and imaging for hEMC**
967

968 4 µL of freshly purified hEMC (in detergent or nanodisc) was applied to glow discharged
969 copper Quantifoil holey carbon grids (R1.2/1.3 300 mesh) at 100% humidity and 4 °C in
970 a Vitrobot Mark IV (Thermo) and incubated for 30 seconds. Excess liquid was blotted
971 away with filter paper (blot force 4 – 6, blot time 4 seconds) and the grid plunge-frozen
972 into liquid ethane. Samples were imaged on a FEI Titan Krios microscope operating at
973 300 kV, equipped with a post-column GIF and a K3 direct detector operating in counting
974 mode. Images were recorded at a nominal magnification of 105,000x (0.8512 Å/pixel at
975 the specimen level) for hEMC in nanodiscs or 81,000x (1.094 Å/pixel at the specimen
976 level) for hEMC in detergent, with target defocus ranging between 0.7 and 2.8 µm and
977 total exposure of ~70 e/Å^2 using SerialEM (Mastronarde, 2005). On-the-fly motion
978 correction, CTF estimation and templated particle auto-picking were performed using a
979 pipeline implemented in Focus (Biyani, 2017).
980

981 **Cloning and expression constructs for hEMC**
982
983 A modified version of the biGBac (Weissmann, 2016) multi-gene cloning method was
984 combined with the BacMam (Goehring, 2014) mammalian expression system to allow for
985 recombinant production of human EMC (hEMC). hEMC subunits were individually
986 inserted into pEG, with EMC5 bearing a C-terminal Flag-tag. To amplify gene-
987 expression cassettes (GEC) from pEG, original forward primers from biGBac were used
988 in combination with modified reverse primers bearing complementarity downstream of
989 the SV40 terminator sequence. GECs were inserted into pBIG1a-e vectors as follows:
990 pBIG1a (EMC1 - Uniprot code Q8N766-1), pBIG1b (EMC4 – Q5J8M3-1; EMC5-Flag –
991 Q8N4V1-1, which encodes DYKDDDDK immediately after R131; EMC6 – Q9BV81),
992 pBIG1c (EMC2 – Q15006; EMC3 – Q9P0I2-1; EMC7 – Q9NPA0), pBIG1d (EMC8 –
993 O43402-1; EMC9 – Q9Y3B6), pBIG1e (EMC10 – Q5UCC4-1). These were
994 subsequently combined into pBIG2abcde to yield a single expression vector containing
995 all ten hEMC subunits. Bacmid was generated in DH10 EMBacY *E. coli* and
996 subsequently transfected into Sf9 insect cells using FuGENE (Promega) reagent. Virus
997 was amplified in Sf9 cells up to P3 and virus supernatant sterilized by filtration.

998 **hEMC expression, purification and nanodisc reconstitution**
999
1000 Recombinant hEMC was expressed by baculovirus transduction of human embryonic
1001 kidney (HEK) 293S GnTI- cells grown in suspension. Cells were maintained at 37 °C in
1002 Freestyle 293 Expression Medium (Thermo) and expanded with home-made suspension
1003 medium (Chaudhary, 2012) in 2 L shaker flasks. For expression of hEMC, 10% (v/v) P3
1004 virus was added to 800 mL of HEK culture at a cell density >3 x 10^6. 16 hours post-
1005 transduction, 10 mM butyrate was added and the temperature reduced to 30 °C. Cells
1006 were harvested 48 hours later and stored frozen at -80 °C.
1007
1008 For purification, 15 – 20 g of cell pellet was thawed and resuspended in 60 – 80 mL Lysis
1009 Buffer containing 50 mM ammonium citrate pH 6.0, 150 mM sodium chloride, 0.001
1010 mg/mL Benzonase, EDTA-free protease inhibitor cocktail (1 tablet per 50 mL of buffer),
1011 and lysed by Dounce homogenization on ice (50 strokes). Glyco-diosgenin (GDN,
1012 Anatrace) was added to the lysate at 2% (w/v) and cellular membranes solubilized for 3

1013 hours at 4 °C under constant stirring. Insolubilized material was removed by
1014 centrifugation at 100,000 x g, supernatant incubated with 2 mL M2 Flag-affinity resin in-
1015 batch for 2 hours at 4 °C. The resin was poured into a column and unbound proteins
1016 washed away with 25 column volumes (CV) of Wash Buffer containing 20 mM
1017 ammonium citrate pH 6.0, 150 mM sodium chloride, 0.01% (w/v) GDN. Bound hEMC
1018 was eluted in 10 CV Wash Buffer containing 0.3 mg/mL Flag peptide and concentrated
1019 to < 500 µL using centrifugal concentration filters with 100 kDa cut—off (Amicon).
1020 Sample was polished using size-exclusion chromatography (SEC) on a Superose 6
1021 Increase 10/300 GL column (GE Healthcare) with Running Buffer containing 10 mM
1022 ammonium citrate pH 6.0, 100 mM sodium chloride, 0.25 mM TCEP, 0.01% (w/v) GDN.
1023 Peak fractions containing hEMC were pooled, concentrated to ~3 mg/mL and used
1024 immediately for cryo-EM grid preparation.
1025
1026 hEMC in nanodiscs composed of MSP1D1 scaffold protein and 1-palmitoyl-2-oleoyl-sn-
1027 glycero-3-phosphatidylcholine (POPC) was reconstituted following Flag-affinity
1028 chromatography. The MSP1D1 expression vector was a gift from Franz Hagn (TUM,
1029 Germany) and the scaffold protein purified from *E. coli* following a published protocol
1030 (Hagn, 2018). Prior to reconstitution, hEMC purified by Flag-affinity chromatography
1031 was mixed with MSP1D1 and POPC (solubilized as 25 mM stock in 5% n-dodecyl β-D-
1032 maltoside) in a 1:4:50 ratio and this mixture incubated on ice for 2 hours. Nanodisc
1033 reconstitution was achieved by incubation with 0.5 - 1 mL Bio-Beads SM-2 (Bio-Rad)
1034 for 16 hours at 4°C under constant rotation. The liquid phase was aspirated, concentrated
1035 to < 500 µL and injected onto a Superose 6 SEC column with buffer containing 10 mM
1036 ammonium citrate pH 6.0, 100 mM sodium chloride, 0.25 mM TCEP, to separate
1037 nanodisc-embedded hEMC from empty nanodiscs. Peak fractions were pooled and
1038 concentrated to ~2 mg/mL for immediate cryo-EM grid preparation.

1039 **Cryo-EM sample preparation and imaging for hEMC**
1040
1041 4 µL of freshly purified hEMC (in detergent or nanodisc) was applied to glow discharged
1042 copper Quantifoil holey carbon grids (R1.2/1.3 300 mesh) at 100% humidity and 4 °C in
1043 a Vitrobot Mark IV (Thermo) and incubated for 30 seconds. Excess liquid was blotted
1044 away with filter paper (blot force 4 – 6, blot time 4 seconds) and the grid plunge-frozen
1045 into liquid ethane. Samples were imaged on a FEI Titan Krios microscope operating at
1046 300 kV, equipped with a post-column GIF and a K3 direct detector operating in counting
1047 mode. Images were recorded at a nominal magnification of 105,000x (0.8512 Å/pixel at
1048 the specimen level) for hEMC in nanodiscs or 81,000x (1.094 Å/pixel at the specimen
1049 level) for hEMC in detergent, with target defocus ranging between 0.7 and 2.8 µm and
1050 total exposure of ~70 e/Å^2 using SerialEM (Mastronarde, 2005). On-the-fly motion
1051 correction, CTF estimation and templated particle auto-picking were performed using a
1052 pipeline implemented in Focus (Biyani, 2017).

1053 **Cryo-EM data processing for hEMC in detergent**
1054
1055 Preprocessing in Focus included dose-weighted motion correction using Motioncor2
1056 (Zheng, 2017), CTF estimation using Gctf (Zhang, 2016) and templated autopicking
1057 using Gautomatch (Kai Zhang). The autopicking template originated from a

reconstruction of hEMC in GDN micelles, with data acquired on a K2 (Gatan) direct electron detector (operated in counting mode) under liquid nitrogen conditions using a Glacios microscope (Thermo) operated at 200 kV. 3713 micrographs with a maximal resolution estimate better than 5 Å were imported into Relion 3.0 (Zivanov, 2018), from which ~3.35 million particles were extracted applying 4-fold binning. These were subjected to three rounds of 2D classification and two rounds of 3D classification (using the reconstruction obtained from the 200kV dataset as reference), followed by 3D autorefinement. This reconstruction was used as initial model for three rounds of 3D classification of the original ~3.35 million particles (first round: K = 10, T = 10; second round: K = 10, T = 10; third round: K = 3, T = 16), yielding a set of 144,222 particles. This set was re-extracted at full pixel size, followed by masked 3D autorefinement, producing a reconstruction at 3.77 Å overall resolution. Application of non-uniform refinement in cryoSPARC (Punjani, 2017; Punjani, 2019) further improved the map quality and overall resolution to 3.60 Å.

Cryo-EM data processing for hEMC in nanodiscs

Micrographs were preprocessed using Focus in a similar manner as for hEMC in detergent. 9164 micrographs with a maximal resolution estimate better than 5 Å were imported into Relion 3.0, from which ~5.9 million particles were extracted applying 4-fold binning. These were subjected to three rounds of 3D classification (using hEMC in GDN as reference for the first round), after which 386739 particles were kept and re-extracted to full pixel size. Particles were aligned using global angular search 3D classification (K = 1, T = 4) before one further round of 3D classification with a soft mask and skipping alignment (K = 6, T = 8), to isolate a set of 177560 homogeneous hEMC particles. Masked 3D autorefinement of this particle set yielded a map at 3.6 Å overall resolution. Implementation of cryoSPARC non-uniform refinement led to a consensus map at 3.4 Å global resolution. To aid de novo model building of cytoplasmic and luminal domains, these parts were subjected to masked focused classification (K = 5, T = 8), 3D autorefinement and post-processing in Relion, yielding improved maps at 3.4 Å and 3.2 Å, respectively. To obtain highest quality maps of the transmembrane domains, the 177560 particles from consensus refinement were processed using Sidesplitter (Ramlaul, 2020), producing a 3.3 Å global map after Relion post-processing, where transmembrane helix pitch and side chains were well resolved and allowed for unambiguous sequence assignment. The final particle set was further subjected to 3D variability analysis (Punjani, 2020) in cryoSPARC, revealing the presence or absence of the EMC7 lumenal domain between the EMC1 beta-propellers. Heterogeneous refinement, using a map from 3D variability analysis containing stronger EMC7 density as reference, allowed for further sub-classification of the consensus particle set. Non-uniform refinement of the class containing stronger EMC7 density produced a map at 3.5 Å global resolution, which was subsequently used to build an EMC7 model.

Model building and refinement of hEMC in nanodiscs and detergent

Given the higher quality hEMC nanodisc map compared to the detergent map, the former was used for de novo model building in Coot (Emsley, 2004; Emsley, 2010). Focused luminal and cytoplasmic, as well as Sideplitter maps, permitted assignment of amino acid

1103 sequence throughout all parts of hEMC. Inspection of structural homology and secondary
1104 structure predictions for the hEMC subunits produced via HHpred and Quick2D servers
1105 (Zimmermann, 2018) predicted the luminal domain of EMC1, the largest hEMC subunit,
1106 to consist of two beta-propellers. EMC7 and EMC10 are predicted to feature beta-
1107 sandwich structures in the lumen. A final missing beta-strand of the EMC1 membrane
1108 proximal propeller could be assigned to the luminal C-terminus of EMC4, which forms a
1109 parallel sheet with EMC1 residues 668 – 674. Almost all of EMC2 is predicted to form
1110 an alpha-solenoid structure harboring several TPR motifs. Analysis of EMC8 and EMC9
1111 amino acid sequences revealed structural homology to CSN5 (deneddylase subunit of the
1112 CSN complex) and Rpn11 (deubiquitinase subunit of the 19S proteasomal regulatory
1113 particle) peptide hydrolase folds. The globular density sitting on the distal face of the
1114 EMC2 solenoid, facing away from the rest of the complex, was modeled with the EMC8
1115 sequence, which shares ~45% amino acid sequence identity with EMC9. Additional
1116 helical density sitting sideways on top of the EMC2 solenoid could be modeled as two
1117 cytoplasmic helices of EMC3 as well as the extended, partially helical meander of the
1118 EMC3 C-terminus. Beta-strand-like density on the EMC8 surface, commonly occupied
1119 by deubiquitinase substrate peptides, was assigned to the extreme N-terminus of EMC4,
1120 with a further downstream part of this cytoplasmic domain snaking along EMC2 and
1121 EMC3 towards the transmembrane part of hEMC.
1122
1123 Clear side-chain resolution and excellent connectivity of the Sidesplitter map, within the
1124 nanodisc encircled membrane domain, allowed us to model all predicted transmembrane
1125 helices of EMC1, EMC3, EMC5 and EMC6. EMC5 extends its C-terminus outside the
1126 membrane, which snakes through the central cavity of the EMC2 solenoid on the
1127 cytoplasmic side. Inspection of the map at lower thresholds revealed density for at least
1128 two additional transmembrane helices facing EMC3 and EMC6 on one side of the
1129 complex: continuous density from one of these helices towards the luminal EMC4 C-
1130 terminus indicates that at least one of these gate helices represent EMC4's C-terminal
1131 transmembrane helix. However, given poor map resolution and connectivity in this
1132 region, we left the other gate helices unassigned.
1133
1134 Model refinement was performed using real-space refinement in Phenix (Adams, 2011),
1135 applying secondary structure and Ramachandran restraints. Initially, luminal and
1136 cytoplasmic domains were refined individually against their focused maps, after which
1137 the improved models were rigid-body placed and refined against the non-uniform refined
1138 consensus map. The transmembrane domain was likewise first refined against the
1139 Sidesplitter map, after which all parts of hEMC were combined into a consensus model
1140 and refined against the consensus map.
1141
1142 The refined hEMC nanodisc model was subsequently docked into the hEMC detergent
1143 map, revealing a relative rotation of the entire lumenal domain. The fitted model was
1144 manually adjusted in Coot (Emsley, 2004; Emsley, 2010) and refined using Phenix real-
1145 space refinement (Adams, 2011). Different masking strategies failed to produce stronger
1146 density for the EMC7 lumenal domain in the hEMC detergent maps, despite EMC7 levels
1147 being comparable to the other hEMC subunits in subsequent mass spectrometry analysis.

1148 EMC7 thus remains absent from our hEMC detergent model, perhaps due to
1149 conformational heterogeneity.
1150
1151 Mass spectrometric analysis of purified hEMC samples in detergent or nanodiscs
1152
1153 GDN solubilized or nanodisc reconstituted hEMC purified by Flag-affinity
1154 chromatography and SEC was subjected to mass spectrometric analysis to assess hEMC
1155 subunit abundance. For reduction and alkylation of the proteins, proteins were incubated
1156 with SDC buffer (1% Sodiumdeoxycholate, 40nmM 2-Cloroacetamide (Sigma-
1157 Aldrich), 10 mM tris(2-carboxyethyl) phosphine (TCEP; PierceTM, Thermo Fisher
1158 Scientific) in 100 mM Tris, pH 8.0) for 20 min at 37 °C. Before digestion the samples
1159 were diluted 1:2 with MS grade water (VWR). Samples were digested overnight at 37 °C
1160 with 1 µg trypsin (Promega).
1161 The solution of peptides was then acidified with Trifluoroacetic acid (Merck) to a final
1162 concentration of 1% and a pH value of < 2, followed by purification via SCX StageTips
1163 (Rappsilber, 2007) washed with 1% TFA in Isopropanol, followed by a second wash with
1164 0.2% TFA, eluted as one fraction with 80% Acetonitrile and 5% Ammonia (Merck).
1165 Samples were vacuum dried and re-suspended in 6 µl of Buffer A (0.1% Formic acid
1166 (Roth) in MS grade water (VWR)).
1167
1168 Purified and desalted peptides were loaded onto a 15-cm column (inner diameter: 75
1169 microns; packed in-house with ReproSil-Pur C18-AQ 1.9-micron beads, Dr. Maisch
1170 GmbH) via the autosampler of the Thermo Easy-nLC 1000 (Thermo Fisher Scientific) at
1171 50 °C. Using the nanoelectrospray interface, eluting peptides were directly sprayed onto
1172 the benchtop Orbitrap mass spectrometer Q Exactive HF (Thermo Fisher Scientific).
1173 Peptides were loaded in buffer A (0.1% (v/v) Formic acid) at 250 nl/min and percentage
1174 of buffer B (80% Acetonitril, 0.1% Formic acid) was ramped to 30% over 45 minutes
1175 followed by a ramp to 60% over 5 minutes then 95% over the next 5 minutes and
1176 maintained at 95% for another 5 minutes. The mass spectrometer was operated in a data-
1177 dependent mode with survey scans from 300 to 1650 m/z (resolution of 60000 at m/z
1178 =200), and up to 10 of the top precursors were selected and fragmented using higher
1179 energy collisional dissociation (HCD with a normalized collision energy of value of 28).
1180 The MS2 spectra were recorded at a resolution of 15000 (at m/z = 200). AGC target for
1181 MS and MS2 scans were set to 3E6 and 1E5 respectively within a maximum injection
1182 time of 100 and 60 ms for MS and MS2 scans respectively. Dynamic exclusion was set to
1183 30ms.
1184
1185 Raw data were processed using the MaxQuant computational platform (Cox, 2008) with
1186 standard settings applied. Shortly, the peak list was searched against the reviewed human
1187 Uniprot database with an allowed precursor mass deviation of 4.5 ppm and an allowed
1188 fragment mass deviation of 20 ppm. MaxQuant by default enables individual peptide
1189 mass tolerances, which was used in the search. Cysteine carbamidomethylation was set as
1190 static modification, and methionine oxidation and N-terminal acetylation as variable
1191 modifications. The iBAQ algorithm was used for calculation of approximate abundances
1192 for the identified proteins (Schwanhäusser, 2011) which normalizes the summed peptide
1193 intensities by the number of theoretically observable peptides of the protein.

1194
1195 **Sequence alignments**
1196
1197 T-coffee PSI-Coffee extension (Notredame, 2000) was used to compute sequence
1198 alignments between yEMC, hEMC, and homologous proteins (**Figure 1 – figure**
1199 **supplement 6-7, Figure 3 – figure supplement 3, Figure 5 – figure supplement 4**).
1200 Outputs of these alignments were visualized in Jalview (Waterhouse, 2009) for figure
1201 creation and colored by ClustalX convention.
1202
1203 **Figure creation**
1204
1205 All figures were assembled and edited in Adobe Illustrator. **Figure 1 and Figure 1 –**
1206 **figure supplement 3** were created using BioRender. All of the visualization and structure
1207 figures were made using UCSF ChimeraX 1.0 (Goddard, 2018) and UCSF Chimera 1.14
1208 (Pettersen, 2004). Flow cytometry plots were generated in Python and labeled in Adobe
1209 Illustrator.
1210

1211 # Acknowledgements

1212 We thank J. Weibazahn, P. Walter, R. Irannejad, J. Gestwicki, H. Nguyen, I. Johnson, N.
1213 Talledge, L. Kenner, E. Thompson, K. Hickey, J. Kellermann, S. von Gronau, M. Feige,
1214 K. Swain, M. Liao, C-W. Lee, F. Wilfling, and members of the Weissman, Frost, and
1215 Schulman laboratories for assistance and helpful discussion; R. Stroud, D.W. Chester,
1216 and S. Aller for assisting with fermentation; M. Sun, H. Autzen, and E. Green for advice
1217 on nanodisc reconstitution; F. Hagn and I. Goba for the gift of the MSP1D1 vector and
1218 advice on nanodisc reconstitution; P. Thomas and D. Asarnow for computational support;
1219 M. Braunfeld, G. Gilbert, E. Tse, D. Bulkley, M. Harrington, A. Myasnikov and Z. Yu of
1220 the UCSF Center for Advanced CryoEM for microscopy support and funded by NIH
1221 grants S10OD020054 and 1S10OD021741; J. Baker-LePain and the QB3 shared cluster
1222 (NIH grant 1S10OD021596-01) for computational support; and the Howard Hughes
1223 Medical Institute (HHMI); Z. Yu and H. Chou of the CryoEM Facility at the HHMI
1224 Janelia Research Campus (NIH grant 1S10OD021596-01). D. Bollschweiler, T. Schäfer
1225 and the cryo-EM facility at the Max Planck Institute of Biochemistry; B. Steigenberger
1226 and the mass spectrometry core facility at the Max Planck Institute of Biochemistry; E.
1227 Gouaux for the gift of the pEG vector; A Titan X Pascal used for this research was
1228 donated by the NVIDIA Corporation. This study was supported in part by the HDFCCC
1229 Laboratory for Cell Analysis Shared Resource Facility through a grant from NIH
1230 (P30CA082103). Molecular graphics and analyses performed with UCSF ChimeraX,
1231 developed by the Resource for Biocomputing, Visualization, and Informatics at the
1232 University of California, San Francisco, with support from National Institutes of Health
1233 R01-GM129325 and the Office of Cyber Infrastructure and Computational Biology,
1234 National Institute of Allergy and Infectious Diseases. UCSF Chimera is developed by the
1235 Resource for Biocomputing, Visualization, and Informatics at the University of
1236 California, San Francisco (supported by NIGMS P41-GM103311).
1237
1238

Funding: Supported by the Peter und Traudl Engelhorn-Stiftung (B.B.); HHMI (J.S.W.), Chan Zuckerberg Biohub and HHMI faculty scholar (A.F.), and by the Deutsche Forschungsgemein-
schaft (DFG, German Research Foundation) – SCHU 3196/1-1 and the Max Planck Society (B.A.S.). M.J.S. is a Howard Hughes Medical Institute Fellow of the Helen Hay Whitney Foundation. N.T.S. was funded by the Whitney Jane Coffin Childs Memorial Fund for Medical Research (Postdoctoral Fellowship). This work was additionally supported by National Institutes of Health P50AI150476 (N.S. and C.S.C.), 1P41CA196276-01 (N.S. and C.S.C.), and 1DP2OD017690-01 (A.F.).

Author contributions: Conception and design, analysis and interpretation of data: L.E.M.V., B.B., K.D.P, N.T.S.O, J.L.B., J.R.P., E.B., N.S., M.J.S., C.S.C, B.A.S, A.F., and J.S.W.; acquisition of data: L.E.M.V., B.B., K.D.P., N.T.S.O., J.L.B., J.R.P., E.B., and N.S.; writing (original draft): L.E.M.V., B.B., and K.D.P.; writing (review and editing): L.E.M.V., B.B., K.D.P, N.T.S.O, J.L.B., J.R.P., E.B., N.S., M.J.S., C.S.C, B.A.S, A.F., and J.S.W

Competing interests: No competing interests.

Data and materials availability: All data needed to evaluate the conclusions in the paper are present in the paper and/or the supplementary materials, and the structural data will be made available in EMPIAR, PDB, and EMDB public databases upon publication. All of the raw data files will be in the supplemental data files and code for evaluating will available at GITHUB (MMMMMMM). Accession numbers are as follows: hEMC nanodisc map (EMD-NNNN) and model (PDB-OOOO); hEMC detergent map (EMD-PPPP) and model (PDB-QQQQ); yEMC nanodisc map (EMD-RRRR) and model(PDB-SSSS); yEMC detergent map (EMD-TTTT).

References

1. Abu-Safieh, L., Alrashed, M., Anazi, S., Alkuraya, H., Khan, A.O., Al-Owain, M., Al-Zahrani, J., Al-Abdi, L., Hashem, M., Al-Tarimi, S., Sebai, M.-A., Shamia, A., Ray-Zack, M.D., Nassan, M., Al-Hassnan, Z.N., Rahbeeni, Z., Waheeb, S., Alkharashi, A., Abboud, E., Al-Hazzaa, S.A.F., Alkuraya, F.S., 2012. Autozygome-guided exome sequencing in retinal dystrophy patients reveals pathogenetic mutations and novel candidate disease genes. Genome Res 23, 236–47. https://doi.org/10.1101/gr.144105.112
2. Adams, P.D., Afonine, P.V., Bunkóczi, G., Chen, V.B., Echols, N., Headd, J.J., Hung, L.-W., Jain, S., Kapral, G.J., Kunstleve, R.W.G., McCoy, A.J., Moriarty, N.W., Oeffner, R.D., Read, R.J., Richardson, D.C., Richardson, J.S., Terwilliger, T.C., Zwart, P.H., 2011. The Phenix software for automated determination of macromolecular structures. Methods 55, 94–106. https://doi.org/10.1016/j.ymeth.2011.07.005
3. Afonine, P.V., Poon, B.K., Read, R.J., Sobolev, O.V., Terwilliger, T.C., Urzhumtsev, A., Adams, P.D., 2018. Real-space refinement in PHENIX for cryo-EM and crystallography. Acta Crystallogr Sect D Struct Biology 74, 531–544. https://doi.org/10.1107/s2059798318006551
4. Amberger JS, Bocchini CA, Scott AF, Hamosh A. OMIM.org: leveraging knowledge across phenotype-gene relationships. Nucleic Acids Res. 2019 Jan 8;47(D1):D1038-D1043. doi:10.1093/nar/gky1151.

5. Anghel, S.A., McGilvray, P.T., Hegde, R.S., Keenan, R.J., 2017. Identification of Oxa1 Homologs Operating in the Eukaryotic Endoplasmic Reticulum. Cell Reports 21, 3708–3716. https://doi.org/10.1016/j.celrep.2017.12.006
6. Asarnow, D., Palovcak, E., Cheng, Y. UCSF pyem v0.5. 2019. Zenodo https://doi.org/10.5281/zenodo.3576630
7. Assimon, V.A., Southworth, D.R., Gestwicki, J.E., 2015. Specific Binding of Tetratricopeptide Repeat Proteins to Heat Shock Protein 70 (Hsp70) and Heat Shock Protein 90 (Hsp90) Is Regulated by Affinity and Phosphorylation. Biochemistry-us 54, 7120–31. https://doi.org/10.1021/acs.biochem.5b00801
8. Bai, L., You, Q., Feng, X., Kovach, A., Li, H., 2020. Structure of the ER membrane complex, a transmembrane-domain insertase. Nature 1–4. https://doi.org/10.1038/s41586-020-2389-3
9. Bagchi, P., Inoue, T., Tsai, B., 2016. EMC1-dependent stabilization drives membrane penetration of a partially destabilized non-enveloped virus. Elife 5, e21470. https://doi.org/10.7554/elife.21470
10. Bircham, P.W., Maass, D.R., Roberts, C.A., Kiew, P.Y., Low, Y.S., Yegambaram, M., Matthews, J., Jack, C.A., Atkinson, P.H., 2011. Secretory pathway genes assessed by high-throughput microscopy and synthetic genetic array analysis. Mol Biosyst 7, 2589. https://doi.org/10.1039/c1mb05175j
11. Biyani, N., Righetto, R.D., McLeod, R., Caujolle-Bert, D., Castano-Diez, D., Goldie, K.N., Stahlberg, H., 2017. Focus: The interface between data collection and data processing in cryo-EM. J Struct Biol 198, 124–133. https://doi.org/10.1016/j.jsb.2017.03.007
12. Blatch, G.L., Lässle, M., 1999. The tetratricopeptide repeat: a structural motif mediating protein-protein interactions. Bioessays 21, 932–939. https://doi.org/10.1002/(sici)1521-1878(199911)21:11<932::aid-bies5>3.0.co;2-n
13. Borowska, M.T., Dominik, P.K., Anghel, S.A., Kossiakoff, A.A., Keenan, R.J., 2015. A YidC-like Protein in the Archaeal Plasma Membrane. Structure 23, 1715–1724. https://doi.org/10.1016/j.str.2015.06.025
14. Chaudhary, S., Pak, J.E., Gruswitz, F., Sharma, V., Stroud, R.M., 2012. Overexpressing human membrane proteins in stably transfected and clonal human embryonic kidney 293S cells. Nat Protoc 7, 453–466. https://doi.org/10.1038/nprot.2011.453
15. Chitwood, P.J., Juszkiewicz, S., Guna, A., Shao, S., Hegde, R.S., 2018. EMC Is Required to Initiate Accurate Membrane Protein Topogenesis. Cell 175, 1507-1519.e16. https://doi.org/10.1016/j.cell.2018.10.009
16. Cho, H., Stanzione, F., Oak, A., Kim, G.H., Yerneni, S., Qi, L., Sum, A.K., Chan, C., 2019. Intrinsic Structural Features of the Human IRE1α Transmembrane Domain Sense Membrane Lipid Saturation. Cell Reports 27, 307-320.e5. https://doi.org/10.1016/j.celrep.2019.03.017
17. Christianson, J.C., Olzmann, J.A., Shaler, T.A., Sowa, M.E., Bennett, E.J., Richter, C.M., Tyler, R.E., Greenblatt, E.J., Harper, J.W., Kopito, R.R., 2012. Defining human ERAD networks through an integrative mapping strategy. Nat Cell Biol 14, 93–105. https://doi.org/10.1038/ncb2383
18. Coelho, J.P.L., Stahl, M., Bloemeke, N., Meighen-Berger, K., Alvira, C.P., Zhang, Z.-R., Sieber, S.A., Feige, M.J., 2019. A network of chaperones prevents and detects failures in membrane protein lipid bilayer integration. Nat Commun 10, 672. https://doi.org/10.1038/s41467-019-08632-0
19. Cornell, C.E., Mileant, A., Thakkar, N., Lee, K.K., Keller, S.L., 2020. Direct imaging of liquid domains in membranes by cryo-electron tomography. Proc National Acad Sci 202002245. https://doi.org/10.1073/pnas.2002245117

20. Corradi, V., Sejdiu, B.I., Mesa-Galloso, H., Abdizadeh, H., Noskov, S.Y., Marrink, S.J., Tieleman, D.P., 2019. Emerging Diversity in Lipid–Protein Interactions. Chem Rev 119, 5775–5848. https://doi.org/10.1021/acs.chemrev.8b00451
21. Costa, E.A., Subramanian, K., Nunnari, J., Weissman, J.S., 2018. Defining the physiological role of SRP in protein-targeting efficiency and specificity. Sci New York N Y 359, 689–692. https://doi.org/10.1126/science.aar3607
22. Cox, J., Mann, M., 2008. MaxQuant enables high peptide identification rates, individualized p.p.b.-range mass accuracies and proteome-wide protein quantification. Nat Biotechnol 26, 1367–1372. https://doi.org/10.1038/nbt.1511
23. Cuff, J.A., Barton, G.J., 2000. Application of multiple sequence alignment profiles to improve protein secondary structure prediction. Proteins Struct Funct Bioinform 40, 502–511. https://doi.org/10.1002/1097-0134(20000815)40:3<502::aid-prot170>3.0.co;2-q
24. Dalbey, R.E., Kuhn, A., 2015. Membrane Insertases Are Present in All Three Domains of Life. Structure 23, 1559–1560. https://doi.org/10.1016/j.str.2015.08.002
25. Diamantopoulou, A., Sun, Z., Mukai, J., Xu, B., Fenelon, K., Karayiorgou, M., Gogos, J.A., 2017. Loss-of-function mutation inMirta22/Emc10rescues specific schizophrenia-related phenotypes in a mouse model of the 22q11.2 deletion. Proc National Acad Sci 114, E6127–E6136. https://doi.org/10.1073/pnas.1615719114
26. Dickinson, M.E., Flenniken, A.M., Ji, X., Teboul, L., Wong, M.D., White, J.K., Meehan, T.F., Weninger, W.J., Westerberg, H., Adissu, H., Baker, C.N., Bower, L., Brown, J.M., Caddle, L.B., Chiani, F., Clary, D., Cleak, J., Daly, M.J., Denegre, J.M., Doe, B., Dolan, M.E., Edie, S.M., Fuchs, H., Gailus-Durner, V., Galli, A., Gambadoro, A., Gallegos, J., Guo, S., Horner, N.R., Hsu, C.-W., Johnson, S.J., Kalaga, S., Keith, L.C., Lanoue, L., Lawson, T.N., Lek, M., Mark, M., Marschall, S., Mason, J., McElwee, M.L., Newbigging, S., Nutter, L.M.J., Peterson, K.A., Ramirez-Solis, R., Rowland, D.J., Ryder, E., Samocha, K.E., Seavitt, J.R., Selloum, M., Szoke-Kovacs, Z., Tamura, M., Trainor, A.G., Tudose, I., Wakana, S., Warren, J., Wendling, O., West, D.B., Wong, L., Yoshiki, A., McKay, M., Urban, B., Lund, C., Froeter, E., LaCasse, T., Mehalow, A., Gordon, E., Donahue, L.R., Taft, R., Kutney, P., Dion, S., Goodwin, L., Kales, S., Urban, R., Palmer, K., Pertuy, F., Bitz, D., Weber, B., Goetz-Reiner, P., Jacobs, H., Marchand, E.L., Amri, A.E., Fertak, L.E., Ennah, H., Ali-Hadji, D., Ayadi, A., Wattenhofer-Donze, M., Jacquot, S., André, P., Birling, M.-C., Pavlovic, G., Sorg, T., Morse, I., Benso, F., Stewart, M.E., Copley, C., Harrison, J., Joynson, S., Guo, R., Qu, D., Spring, S., Yu, L., Ellegood, J., Morikawa, L., Shang, X., Feugas, P., Creighton, A., Penton, P.C., Danisment, O., Griggs, N., Tudor, C.L., Green, A.L., Mazzeo, C.I., Siragher, E., Lillistone, C., Tuck, E., Gleeson, D., Sethi, D., Bayzetinova, T., Burvill, J., Habib, B., Weavers, L., Maswood, R., Miklejewska, E., Woods, M., Grau, E., Newman, S., Sinclair, C., Brown, E., Ayabe, S., Iwama, M., Murakami, A., Wurst, W., MacArthur, D.G., Tocchini-Valentini, G.P., Gao, X., Flicek, P., Bradley, A., Skarnes, W.C., Justice, M.J., Parkinson, H.E., Moore, M., Wells, S., Braun, R.E., Svenson, K.L., Angelis, M.H. de, Herault, Y., Mohun, T., Mallon, A.-M., Henkelman, R.M., Brown, S.D.M., Adams, D.J., Lloyd, K.C.K., McKerlie, C., Beaudet, A.L., Bućan, M., Murray, S.A., 2016. High-throughput discovery of novel developmental phenotypes. Nature 537, 508–514. https://doi.org/10.1038/nature19356 https://www.mousephenotype.org/publications/
27. Ellgaard, L., McCaul, N., Chatsisvili, A., Braakman, I., 2016. Co- and Post-Translational Protein Folding in the ER: Co- and Post-Translational Protein Folding in the ER. Traffic 17, 615–638. https://doi.org/10.1111/tra.12392
28. Emsley, P., Cowtan, K., 2004. Coot: model-building tools for molecular graphics. Acta Crystallogr Sect D Biological Crystallogr 60, 2126–2132. https://doi.org/10.1107/s0907444904019158

29. Emsley, P., Lohkamp, B., Scott, W.G., Cowtan, K., 2010. Features and development of Coot. Acta Crystallogr Sect D Biological Crystallogr 66, 486–501. https://doi.org/10.1107/s0907444910007493
30. Goddard, T.D., Huang, C.C., Meng, E.C., Pettersen, E.F., Couch, G.S., Morris, J.H., Ferrin, T.E., 2018. UCSF ChimeraX: Meeting modern challenges in visualization and analysis. Protein Sci 27, 14–25. https://doi.org/10.1002/pro.3235
31. Goehring, A., Lee, C.-H., Wang, K.H., Michel, J.C., Claxton, D.P., Baconguis, I., Althoff, T., Fischer, S., Garcia, K.C., Gouaux, E., 2014. Screening and large-scale expression of membrane proteins in mammalian cells for structural studies. Nat Protoc 9, 2574–2585. https://doi.org/10.1038/nprot.2014.173
32. Graham, J.B., Canniff, N.P., Hebert, D.N., 2019. TPR-containing proteins control protein organization and homeostasis for the endoplasmic reticulum. Crit Rev Biochem Mol 54, 103–118. https://doi.org/10.1080/10409238.2019.1590305
33. Guna, A., Volkmar, N., Christianson, J.C., Hegde, R.S., 2017. The ER membrane protein complex is a transmembrane domain insertase. Science 359, 470–473. https://doi.org/10.1126/science.aao3099
34. Hagn, F., Nasr, M.L., Wagner, G., 2018. Assembly of phospholipid nanodiscs of controlled size for structural studies of membrane proteins by NMR. Nat Protoc 13, 79–98. https://doi.org/10.1038/nprot.2017.094
35. Halbleib, K., Pesek, K., Covino, R., Hofbauer, H.F., Wunnicke, D., Hänelt, I., Hummer, G., Ernst, R., 2017. Activation of the Unfolded Protein Response by Lipid Bilayer Stress. Mol Cell 67, 673-684.e8. https://doi.org/10.1016/j.molcel.2017.06.012
36. Harel, T., Yesil, G., Bayram, Y., Coban-Akdemir, Z., Charng, W.-L., Karaca, E., Asmari, A.A., Eldomery, M.K., Hunter, J.V., Jhangiani, S.N., Rosenfeld, J.A., Pehlivan, D., El-Hattab, A.W., Saleh, M.A., LeDuc, C.A., Muzny, D., Boerwinkle, E., Genomics, B.-H.C. for M., Gibbs, R.A., Chung, W.K., Yang, Y., Belmont, J.W., Lupski, J.R., 2016. Monoallelic and Biallelic Variants in EMC1 Identified in Individuals with Global Developmental Delay, Hypotonia, Scoliosis, and Cerebellar Atrophy. Am J Hum Genet 98, 562–70. https://doi.org/10.1016/j.ajhg.2016.01.011
37. Heberle, F.A., Doktorova, M., Scott, H.L., Skinkle, A.D., Waxham, M.N., Levental, I., 2020. Direct label-free imaging of nanodomains in biomimetic and biological membranes by cryogenic electron microscopy. Proc National Acad Sci 202002200. https://doi.org/10.1073/pnas.2002200117
38. Hiramatsu, N., Tago, T., Satoh, T., Satoh, A.K., 2019. ER membrane protein complex is required for the insertions of late-synthesized transmembrane helices of Rh1 in Drosophila photoreceptors. Mol Biol Cell 30, 2890–2900. https://doi.org/10.1091/mbc.e19-08-0434
39. Hofbauer, H.F., Gecht, M., Fischer, S.C., Seybert, A., Frangakis, A.S., Stelzer, E.H.K., Covino, R., Hummer, G., Ernst, R., 2018. The molecular recognition of phosphatidic acid by an amphipathic helix in Opi1Headgroup selectivity of an amphipathic helix. J Cell Biology 217, 3109–3126. https://doi.org/10.1083/jcb.201802027
40. Hu, M., Yu, H., Gu, K., Wang, Z., Ruan, H., Wang, K., Ren, S., Li, B., Gan, L., Xu, S., Yang, G., Shen, Y., Li, X., 2018. A particle-filter framework for robust cryo-EM 3D reconstruction. Nat Methods 15, 1083–1089. https://doi.org/10.1038/s41592-018-0223-8
41. Jacquemyn, J., Cascalho, A., Goodchild, R.E., 2017. The ins and outs of endoplasmic reticulum-controlled lipid biosynthesis. Embo Rep 18, 1905–1921. https://doi.org/10.15252/embr.20164342
42. Jones, D.T., 1999. Protein secondary structure prediction based on position-specific scoring matrices. J Mol Biol 292, 195–202. https://doi.org/10.1006/jmbi.1999.3091

43. Jones, D.T., Taylor, W.R., Thornton, J.M., 1994. A Model Recognition Approach to the Prediction of All-Helical Membrane Protein Structure and Topology. Biochemistry-us 33, 3038–3049. https://doi.org/10.1021/bi00176a037
44. Jonikas, M.C., Collins, S.R., Denic, V., Oh, E., Quan, E.M., Schmid, V., Weibezahn, J., Schwappach, B., Walter, P., Weissman, J.S., Schuldiner, M., 2009. Comprehensive characterization of genes required for protein folding in the endoplasmic reticulum. Sci New York N Y 323, 1693–7. https://doi.org/10.1126/science.1167983
45. Junes-Gill, K.S., Gallaher, T.K., Gluzman-Poltorak, Z., Miller, J.D., Wheeler, C.J., Fan, X., Basile, L.A., 2010. hHSS1: a novel secreted factor and suppressor of glioma growth located at chromosome 19q13.33. J Neuro-oncol 102, 197–211. https://doi.org/10.1007/s11060-010-0314-6
46. Källberg, M., Wang, H., Wang, S., Peng, J., Wang, Z., Lu, H., Xu, J., 2012. Template-based protein structure modeling using the RaptorX web server. Nat Protoc 7, 1511–1522. https://doi.org/10.1038/nprot.2012.085
47. Kelley, L.A., Mezulis, S., Yates, C.M., Wass, M.N., Sternberg, M.J.E., 2015. The Phyre2 web portal for protein modeling, prediction and analysis. Nat Protoc 10, 845–858. https://doi.org/10.1038/nprot.2015.053
48. Kim J, Stroud RM, Craik CS. Rapid identification of recombinant Fabs that bind to membrane proteins. *Methods*. 2011;55(4):303-309. doi:10.1016/j.ymeth.2011.09.012
49. Kimanius, D., Forsberg, B.O., Scheres, S.H., Lindahl, E., 2016. Accelerated cryo-EM structure determination with parallelisation using GPUs in RELION-2. Elife 5, e18722. https://doi.org/10.7554/elife.18722
50. Krogh, A., Larsson, B., Heijne, G. von, Sonnhammer, E.L.L., 2001. Predicting transmembrane protein topology with a hidden markov model: application to complete genomes. J Mol Biol 305, 567–580. https://doi.org/10.1006/jmbi.2000.4315
51. Krysztofinska, E.M., Evans, N.J., Thapaliya, A., Murray, J.W., Morgan, R.M.L., Martinez-Lumbreras, S., Isaacson, R.L., 2017. Structure and Interactions of the TPR Domain of Sgt2 with Yeast Chaperones and Ybr137wp. Frontiers Mol Biosci 4, 68. https://doi.org/10.3389/fmolb.2017.00068
52. Kudze, T., Mendez-Dorantes, C., Jalloh, C.S., McClellan, A.J., 2018. Evidence for interaction between Hsp90 and the ER membrane complex. Cell Stress Chaperones 23, 1101–1115. https://doi.org/10.1007/s12192-018-0908-z
53. Kumazaki, K., Kishimoto, T., Furukawa, A., Mori, H., Tanaka, Y., Dohmae, N., Ishitani, R., Tsukazaki, T., Nureki, O., 2014. Crystal structure of Escherichia coli YidC, a membrane protein chaperone and insertase. Sci Rep-uk 4, 7299. https://doi.org/10.1038/srep07299
54. Lahiri, S., Chao, J.T., Tavassoli, S., Wong, A.K.O., Choudhary, V., Young, B.P., Loewen, C.J.R., Prinz, W.A., 2014. A conserved endoplasmic reticulum membrane protein complex (EMC) facilitates phospholipid transfer from the ER to mitochondria. Plos Biol 12, e1001969. https://doi.org/10.1371/journal.pbio.1001969
55. Laverty, D., Desai, R., Uchański, T., Masiulis, S., Stec, W.J., Malinauskas, T., Zivanov, J., Pardon, E., Steyaert, J., Miller, K.W., Aricescu, A.R., 2019. Cryo-EM structure of the human α1β3γ2 GABAA receptor in a lipid bilayer. Nature 565, 516–520. https://doi.org/10.1038/s41586-018-0833-4
56. Lin, D.L., Inoue, T., Chen, Y.-J., Chang, A., Tsai, B., Tai, A.W., 2019. The ER Membrane Protein Complex Promotes Biogenesis of Dengue and Zika Virus Non-structural Multi-pass Transmembrane Proteins to Support Infection. Cell Reports 27, 1666-1674.e4. https://doi.org/10.1016/j.celrep.2019.04.051
57. Louie, R.J., Guo, J., Rodgers, J.W., White, R., Shah, N.A., Pagant, S., Kim, P., Livstone, M., Dolinski, K., McKinney, B.A., Hong, J., Sorscher, E.J., Bryan, J., Miller, E.A., Hartman, J.L., 2012. A yeast phenomic model for the gene interaction network

modulating CFTR-ΔF508 protein biogenesis. Genome Med 4, 103. https://doi.org/10.1186/gm404

58. Li, X., Mooney, P., Zheng, S., Booth, C.R., Braunfeld, M.B., Gubbens, S., Agard, D.A., Cheng, Y., 2013. Electron counting and beam-induced motion correction enable near-atomic-resolution single-particle cryo-EM. Nat Methods 10, 584–590. https://doi.org/10.1038/nmeth.2472
59. Liebschner, D., Afonine, P.V., Baker, M.L., Bunkóczi, G., Chen, V.B., Croll, T.I., Hintze, B., Hung, L.-W., Jain, S., McCoy, A.J., Moriarty, N.W., Oeffner, R.D., Poon, B.K., Prisant, M.G., Read, R.J., Richardson, J.S., Richardson, D.C., Sammito, M.D., Sobolev, O.V., Stockwell, D.H., Terwilliger, T.C., Urzhumtsev, A.G., Videau, L.L., Williams, C.J., Adams, P.D., 2019. Macromolecular structure determination using X-rays, neutrons and electrons: recent developments in Phenix. Acta Crystallogr Sect D 75, 861–877. https://doi.org/10.1107/s2059798319011471
60. Luo, W., Gong, X., Chang, A., 2002. An ER Membrane Protein, Sop4, Facilitates ER Export of the Yeast Plasma Membrane [H+]ATPase, Pma1. Traffic 3, 730–739. https://doi.org/10.1034/j.1600-0854.2002.31005.x
61. Lupas, A., Dyke, M.V., Stock, J., 1991. Predicting coiled coils from protein sequences. Science 252, 1162–1164. https://doi.org/10.1126/science.252.5009.1162
62. Marinko, J.T., Huang, H., Penn, W.D., Capra, J.A., Schlebach, J.P., Sanders, C.R., 2019. Folding and Misfolding of Human Membrane Proteins in Health and Disease: From Single Molecules to Cellular Proteostasis. Chem Rev 119, 5537–5606. https://doi.org/10.1021/acs.chemrev.8b00532
63. Marquez, J., Criscione, J., Charney, R.M., Prasad, M.S., Hwang, W.Y., Mis, E.K., García-Castro, M.I., Khokha, M.K., 2020. Disrupted ER membrane protein complex-mediated topogenesis drives congenital neural crest defects. J Clin Invest 130, 813–826. https://doi.org/10.1172/jci129308
64. Mastronarde, D.N., 2005. Automated electron microscope tomography using robust prediction of specimen movements. J Struct Biol 152, 36–51. https://doi.org/10.1016/j.jsb.2005.07.007
65. Mitra, K., Ubarretxena-Belandia, I., Taguchi, T., Warren, G., Engelman, D.M., 2004. Modulation of the bilayer thickness of exocytic pathway membranes by membrane proteins rather than cholesterol. Proc National Acad Sci 101, 4083–4088. https://doi.org/10.1073/pnas.0307332101
66. Morin, A., Eisenbraun, B., Key, J., Sanschagrin, P.C., Timony, M.A., Ottaviano, M., Sliz, P., 2013. Collaboration gets the most out of software. Elife 2, e01456. https://doi.org/10.7554/elife.01456
67. Ngo, A.M., Shurtleff, M.J., Popova, K.D., Kulsuptrakul, J., Weissman, J.S., Puschnik, A.S., 2019. The ER membrane protein complex is required to ensure correct topology and stable expression of flavivirus polyproteins. Elife 8, e48469. https://doi.org/10.7554/elife.48469
68. Notredame, C., Higgins, D.G., Heringa, J., 2000. T-coffee: a novel method for fast and accurate multiple sequence alignment. J Mol Biol 302, 205–217. https://doi.org/10.1006/jmbi.2000.4042
69. O'Donnell, J.P., Phillips, B.P., Yagita, Y., Juszkiewicz, S., Wagner, A., Malinverni, D., Keenan, R.J., Miller, E.A., Hegde, R.S., 2020. The architecture of EMC reveals a path for membrane protein insertion. Elife 9, e57887. https://doi.org/10.7554/elife.57887
70. Obradovic, Z., Peng, K., Vucetic, S., Radivojac, P., Dunker, A.K., 2005. Exploiting heterogeneous sequence properties improves prediction of protein disorder. Proteins Struct Funct Bioinform 61, 176–182. https://doi.org/10.1002/prot.20735
71. Ouali, M., King, R.D., 2000. Cascaded multiple classifiers for secondary structure prediction. Protein Sci 9, 1162–1176. https://doi.org/10.1110/ps.9.6.1162

72. Peng, K., Radivojac, P., Vucetic, S., Dunker, A.K., Obradovic, Z., 2006. Length-dependent prediction of protein intrinsic disorder. Bmc Bioinformatics 7, 208. https://doi.org/10.1186/1471-2105-7-208
73. Petkovic, M., Oses-Prieto, J., Burlingame, A., Jan, L.Y., Jan, Y.N., 2020. TMEM16K is an interorganelle regulator of endosomal sorting. Nat Commun 11, 3298. https://doi.org/10.1038/s41467-020-17016-8
74. Pettersen, E.F., Goddard, T.D., Huang, C.C., Couch, G.S., Greenblatt, D.M., Meng, E.C., Ferrin, T.E., 2004. UCSF Chimera—A visualization system for exploratory research and analysis. J Comput Chem 25, 1605–1612. https://doi.org/10.1002/jcc.20084
75. Pfeffer, S., Dudek, J., Schaffer, M., Ng, B.G., Albert, S., Plitzko, J.M., Baumeister, W., Zimmermann, R., Freeze, H.H., Engel, B.D., Förster, F., 2017. Dissecting the molecular organization of the translocon-associated protein complex. Nat Commun 8, 14516. https://doi.org/10.1038/ncomms14516
76. Pleiner, T., Tomaleri, G.P., Januszyk, K., Inglis, A.J., Hazu, M., Voorhees, R.M., 2020. Structural basis for membrane insertion by the human ER membrane protein complex. Science eabb5008. https://doi.org/10.1126/science.abb5008
77. Probert, F., Rice, P., Scudamore, C.L., Wells, S., Williams, R., Hough, T.A., Cox, I.J., 2015. 1H NMR Metabolic Profiling of Plasma Reveals Additional Phenotypes in Knockout Mouse Models. J Proteome Res 14, 2036–2045. https://doi.org/10.1021/pr501039k
78. Punjani, A., Rubinstein, J.L., Fleet, D.J., Brubaker, M.A., 2017. cryoSPARC: algorithms for rapid unsupervised cryo-EM structure determination. Nat Methods 14, 290–296. https://doi.org/10.1038/nmeth.4169
79. Punjani, A., Zhang, H., Fleet, D.J., 2019. Non-uniform refinement: Adaptive regularization improves single particle cryo-EM reconstruction. Biorxiv 2019.12.15.877092. https://doi.org/10.1101/2019.12.15.877092
80. Punjani, A., Fleet, D.J., 2020. 3D Variability Analysis: Directly resolving continuous flexibility and discrete heterogeneity from single particle cryo-EM images. Biorxiv 2020.04.08.032466. https://doi.org/10.1101/2020.04.08.032466
81. Raman, S., Vernon, R., Thompson, J., Tyka, M., Sadreyev, R., Pei, J., Kim, D., Kellogg, E., DiMaio, F., Lange, O., Kinch, L., Sheffler, W., Kim, B., Das, R., Grishin, N.V., Baker, D., 2009. Structure prediction for CASP8 with all-atom refinement using Rosetta. Proteins Struct Funct Bioinform 77, 89–99. https://doi.org/10.1002/prot.22540
82. Ramírez, A.S., Kowal, J., Locher, K.P., 2019. Cryo–electron microscopy structures of human oligosaccharyltransferase complexes OST-A and OST-B. Science 366, 1372–1375. https://doi.org/10.1126/science.aaz3505
83. Ramlaul, K., Palmer, C.M., Nakane, T., Aylett, C.H.S., 2020. Mitigating local over-fitting during single particle reconstruction with SIDESPLITTER. J Struct Biol 211, 107545. https://doi.org/10.1016/j.jsb.2020.107545
84. Rappsilber, J., Mann, M., Ishihama, Y., 2007. Protocol for micro-purification, enrichment, pre-fractionation and storage of peptides for proteomics using StageTips. Nat Protoc 2, 1896–1906. https://doi.org/10.1038/nprot.2007.261
85. Reinisch, K.M., Camilli, P.D., 2015. SMP-domain proteins at membrane contact sites: Structure and function. Biochim Biophys Acta 1861, 924–7. https://doi.org/10.1016/j.bbalip.2015.12.003
86. Richard, M., Boulin, T., Robert, V.J.P., Richmond, J.E., Bessereau, J.-L., 2013. Biosynthesis of ionotropic acetylcholine receptors requires the evolutionarily conserved ER membrane complex. Proc National Acad Sci 110, E1055–E1063. https://doi.org/10.1073/pnas.1216154110
87. Ritchie, T.K., Grinkova, Y.V., Bayburt, T.H., Denisov, I.G., Zolnerciks, J.K., Atkins, W.M., Sligar, S.G., 2009. Chapter Eleven Reconstitution of Membrane Proteins in

Phospholipid Bilayer Nanodiscs. Methods Enzymol 464, 211–231. https://doi.org/10.1016/s0076-6879(09)64011-8

88. Rost, B., 2001. Review: Protein Secondary Structure Prediction Continues to Rise. J Struct Biol 134, 204–218. https://doi.org/10.1006/jsbi.2001.4336
89. Rothstein, R., 1991. [19] Targeting, disruption, replacement, and allele rescue: Integrative DNA transformation in yeast. Methods Enzymol 194, 281–301. https://doi.org/10.1016/0076-6879(91)94022-5
90. Roy, A., Kucukural, A., Zhang, Y., 2010. I-TASSER: a unified platform for automated protein structure and function prediction. Nat Protoc 5, 725–738. https://doi.org/10.1038/nprot.2010.5
91. Salas-Estrada, L.A., Leioatts, N., Romo, T.D., Grossfield, A., 2018. Lipids Alter Rhodopsin Function via Ligand-like and Solvent-like Interactions. Biophys J 114, 355–367. https://doi.org/10.1016/j.bpj.2017.11.021
92. Samuelson, J.C., Chen, M., Jiang, F., Möller, I., Wiedmann, M., Kuhn, A., Phillips, G.J., Dalbey, R.E., 2000. YidC mediates membrane protein insertion in bacteria. Nature 406, 637–641. https://doi.org/10.1038/35020586
93. Satoh, T., Ohba, A., Liu, Z., Inagaki, T., Satoh, A.K., 2015. dPob/EMC is essential for biosynthesis of rhodopsin and other multi-pass membrane proteins in Drosophila photoreceptors. Elife 4, e06306. https://doi.org/10.7554/elife.06306
94. Savidis, G., McDougall, W.M., Meraner, P., Perreira, J.M., Portmann, J.M., Trincucci, G., John, S.P., Aker, A.M., Renzette, N., Robbins, D.R., Guo, Z., Green, S., Kowalik, T.F., Brass, A.L., 2016. Identification of Zika Virus and Dengue Virus Dependency Factors using Functional Genomics. Cell Reports 16, 232–246. https://doi.org/10.1016/j.celrep.2016.06.028
95. Scheufler, C., Brinker, A., Bourenkov, G., Pegoraro, S., Moroder, L., Bartunik, H., Hartl, F.U., Moarefi, I., 2000. Structure of TPR Domain–Peptide Complexes Critical Elements in the Assembly of the Hsp70–Hsp90 Multichaperone Machine. Cell 101, 199–210. https://doi.org/10.1016/s0092-8674(00)80830-2
96. Schlegel, T., Mirus, O., Haeseler, A. von, Schleiff, E., 2007. The Tetratricopeptide Repeats of Receptors Involved in Protein Translocation across Membranes. Mol Biol Evol 24, 2763–2774. https://doi.org/10.1093/molbev/msm211
97. Schwanhäusser, B., Busse, D., Li, N., Dittmar, G., Schuchhardt, J., Wolf, J., Chen, W., Selbach, M., 2011. Global quantification of mammalian gene expression control. Nature 473, 337–342. https://doi.org/10.1038/nature10098
98. Sejdiu, B.I., Tieleman, D.P., 2020. Lipid-Protein Interactions Are a Unique Property and Defining Feature of G Protein-Coupled Receptors. Biophys J 118, 1887–1900. https://doi.org/10.1016/j.bpj.2020.03.008
99. Shaikh, T.R., Gao, H., Baxter, W.T., Asturias, F.J., Boisset, N., Leith, A., Frank, J., 2008. SPIDER image processing for single-particle reconstruction of biological macromolecules from electron micrographs. Nat Protoc 3, 1941–1974. https://doi.org/10.1038/nprot.2008.156
100. Shurtleff, M.J., Itzhak, D.N., Hussmann, J.A., Oakdale, N.T.S., Costa, E.A., Jonikas, M., Weibezahn, J., Popova, K.D., Jan, C.H., Sinitcyn, P., Vembar, S.S., Hernandez, H., Cox, J., Burlingame, A.L., Brodsky, J.L., Frost, A., Borner, G.H., Weissman, J.S., 2018. The ER membrane protein complex interacts cotranslationally to enable biogenesis of multipass membrane proteins. Elife 7, e37018. https://doi.org/10.7554/elife.37018
101. Song, Y., DiMaio, F., Wang, R.Y.-R., Kim, D., Miles, C., Brunette, T., Thompson, J., Baker, D., 2013. High-Resolution Comparative Modeling with RosettaCM. Structure 21, 1735–1742. https://doi.org/10.1016/j.str.2013.08.005

102. Stagg, S.M., Noble, A.J., Spilman, M., Chapman, M.S., 2014. ResLog plots as an empirical metric of the quality of cryo-EM reconstructions. J Struct Biol 185, 418–426. https://doi.org/10.1016/j.jsb.2013.12.010

103. Suloway, C.J.M., Chartron, J.W., Zaslaver, M., Clemons, W.M., 2009. Model for eukaryotic tail-anchored protein binding based on the structure of Get3. Proc National Acad Sci 106, 14849–14854. https://doi.org/10.1073/pnas.0907522106

104. Talbot, B.E., Vandorpe, D.H., Stotter, B.R., Alper, S.L., Schlondorff, J.S., 2019. Transmembrane insertases and N-glycosylation critically determine synthesis, trafficking, and activity of the nonselective cation channel TRPC6. J Biol Chem 294, 12655–12669. https://doi.org/10.1074/jbc.ra119.008299

105. Tang, X., Snowball, J.M., Xu, Y., Na, C.-L., Weaver, T.E., Clair, G., Kyle, J.E., Zink, E.M., Ansong, C., Wei, W., Huang, M., Lin, X., Whitsett, J.A., 2017. EMC3 coordinates surfactant protein and lipid homeostasis required for respiration. J Clin Invest 127, 4314–4325. https://doi.org/10.1172/jci94152

106. Tian, S., Wu, Q., Zhou, B., Choi, M.Y., Ding, B., Yang, W., Dong, M., 2019. Proteomic Analysis Identifies Membrane Proteins Dependent on the ER Membrane Protein Complex. Cell Reports 28, 2517-2526.e5. https://doi.org/10.1016/j.celrep.2019.08.006

107. Volkmar, N., Thezenas, M.-L., Louie, S.M., Juszkiewicz, S., Nomura, D.K., Hegde, R.S., Kessler, B.M., Christianson, J.C., 2018. The ER membrane protein complex promotes biogenesis of sterol-related enzymes maintaining cholesterol homeostasis. J Cell Sci 132, jcs223453. https://doi.org/10.1242/jcs.223453

108. Volkmar, N., Christianson, J.C., 2020. Squaring the EMC – how promoting membrane protein biogenesis impacts cellular functions and organismal homeostasis. J Cell Sci 133, jcs243519. https://doi.org/10.1242/jcs.243519

109. Volmer, R., Ploeg, K. van der, Ron, D., 2013. Membrane lipid saturation activates endoplasmic reticulum unfolded protein response transducers through their transmembrane domains. Proc National Acad Sci 110, 4628–4633. https://doi.org/10.1073/pnas.1217611110

110. Vyas, N.K., Vyas, M.N., Chervenak, M.C., Johnson, M.A., Pinto, B.M., Bundle, D.R., Quiocho, F.A., 2002. Molecular Recognition of Oligosaccharide Epitopes by a Monoclonal Fab Specific for Shigella flexneri Y Lipopolysaccharide: X-ray Structures and Thermodynamics. Biochemistry-us 41, 13575–13586. https://doi.org/10.1021/bi0261387

111. Ward, J.J., Sodhi, J.S., McGuffin, L.J., Buxton, B.F., Jones, D.T., 2004. Prediction and Functional Analysis of Native Disorder in Proteins from the Three Kingdoms of Life. J Mol Biol 337, 635–645. https://doi.org/10.1016/j.jmb.2004.02.002

112. Wainberg, M., Kamber, R.A., Balsubramani, A., Meyers, R.M., Sinnott-Armstrong, N., Hornburg, D., Jiang, L., Chan, J., Jian, R., Gu, M., Shcherbina, A., Dubreuil, M.M., Spees, K., Snyder, M.P., Kundaje, A., Bassik, M.C., 2019. A genome-wide almanac of co-essential modules assigns function to uncharacterized genes. Biorxiv 827071. https://doi.org/10.1101/827071

113. Waterhouse, A.M., Procter, J.B., Martin, D.M.A., Clamp, M., Barton, G.J., 2009. Jalview Version 2—a multiple sequence alignment editor and analysis workbench. Bioinformatics 25, 1189–1191. https://doi.org/10.1093/bioinformatics/btp033

114. Weissmann, F., Petzold, G., VanderLinden, R., Veld, P.J.H. in ’t, Brown, N.G., Lampert, F., Westermann, S., Stark, H., Schulman, B.A., Peters, J.-M., 2016. biGBac enables rapid gene assembly for the expression of large multisubunit protein complexes. Proc National Acad Sci 113, E2564–E2569. https://doi.org/10.1073/pnas.1604935113

115. Wideman, J.G., 2015. The ubiquitous and ancient ER membrane protein complex (EMC): tether or not? F1000research 4, 624. https://doi.org/10.12688/f1000research.6944.1

116. Wu, S., Avila-Sakar, A., Kim, J., Booth, D.S., Greenberg, C.H., Rossi, A., Liao, M., Li, X., Alian, A., Griner, S.L., Juge, N., Yu, Y., Mergel, C.M., Chaparro-Riggers, J., Strop, P., Tampé, R., Edwards, R.H., Stroud, R.M., Craik, C.S., Cheng, Y., 2012. Fabs Enable Single Particle cryoEM Studies of Small Proteins. Structure 20, 582–592. https://doi.org/10.1016/j.str.2012.02.017

117. Xiong, L., Zhang, L., Yang, Y., Li, N., Lai, W., Wang, F., Zhu, X., Wang, T., 2020. ER complex proteins are required for rhodopsin biosynthesis and photoreceptor survival in Drosophila and mice. Cell Death Differ 27, 646–661. https://doi.org/10.1038/s41418-019-0378-6

118. Yang, J., Yan, R., Roy, A., Xu, D., Poisson, J., Zhang, Y., 2015. The I-TASSER Suite: protein structure and function prediction. Nat Methods 12, 7–8. https://doi.org/10.1038/nmeth.3213

119. Zhang, K., 2016. Gctf: Real-time CTF determination and correction. J Struct Biol 193, 1–12. https://doi.org/10.1016/j.jsb.2015.11.003

120. Zhang, S., Xu, C., Larrimore, K.E., Ng, D.T.W., 2017. Slp1-Emp65: A Guardian Factor that Protects Folding Polypeptides from Promiscuous Degradation. Cell 171, 346-357.e12. https://doi.org/10.1016/j.cell.2017.08.036

121. Zhang, Y., 2008. I-TASSER server for protein 3D structure prediction. Bmc Bioinformatics 9, 40. https://doi.org/10.1186/1471-2105-9-40

122. Zheng, S.Q., Palovcak, E., Armache, J.-P., Verba, K.A., Cheng, Y., Agard, D.A., 2017. MotionCor2: anisotropic correction of beam-induced motion for improved cryo-electron microscopy. Nat Methods 14, 331–332. https://doi.org/10.1038/nmeth.4193

123. Zhou, Y., Wu, F., Zhang, M., Xiong, Z., Yin, Q., Ru, Y., Shi, H., Li, J., Mao, S., Li, Y., Cao, X., Hu, R., Liew, C.W., Ding, Q., Wang, X., Zhang, Y., 2018. EMC10 governs male fertility via maintaining sperm ion balance. J Mol Cell Biol 10, 503–514. https://doi.org/10.1093/jmcb/mjy024

124. Zimmermann, L., Stephens, A., Nam, S.-Z., Rau, D., Kübler, J., Lozajic, M., Gabler, F., Söding, J., Lupas, A.N., Alva, V., 2017. A Completely Reimplemented MPI Bioinformatics Toolkit with a New HHpred Server at its Core. J Mol Biol 430, 2237–2243. https://doi.org/10.1016/j.jmb.2017.12.007

125. Zivanov, J., Nakane, T., Forsberg, B.O., Kimanius, D., Hagen, W.J., Lindahl, E., Scheres, S.H., 2018. New tools for automated high-resolution cryo-EM structure determination in RELION-3. Elife 7, e42166. https://doi.org/10.7554/elife.42166